Naval Research Laboratory

Washington, DC 20375-5320

Theory and Simulation of a Field Emission Microtriode: Analysis and Incorporation into Macroscopic Device Characterization
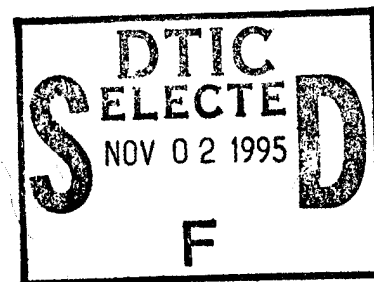
K.L. Jensen
E.G. Zaidman
M.A. Kodis

Vacuum Electronics Branch
Electronics Science and Technology Division

B. Goplen
D.N. Smithe

Mission Research Corporation
Newington, VA

DTIC
SELECTED
NOV 0 2 1995
F

October 12, 1995

19951030 126

DTIC QUALITY INSPECTED 5

REPORT DOCUMENTATION PAGE

Public reporting burden for this collection of information is estimated to average 1 hour per response, including the time for reviewing instructions, searching existing data sources, gathering and maintaining the data needed, and completing and reviewing the collection of information. Send comments regarding this burden estimate or any other aspect of this collection of information, including suggestions for reducing this burden, to Washington Headquarters Services, Directorate for Information Operations and Reports, 1215 Jefferson Davis Highway, Suite 1204, Arlington, VA 22202-4302, and to the Office of Management and Budget. Paperwork Reduction Project (0704-0188), Washington, DC 20503.

1. AGENCY USE ONLY (Leave Blank)	2. REPORT DATE October 12, 1995	3. REPORT TYPE AND DATES COVERED Interim Report — Sept. 1994-Sept. 1995	
4. TITLE AND SUBTITLE Theory and Simulation of a Gated Field Emitter: Analysis and Incorporation into Macroscopic Device Characterization			**5. FUNDING NUMBERS** PE — 0602234N ONR — R534R54
6. AUTHOR(S) K.L. Jensen, E.G. Zaidman, M.A. Kodis, B. Goplen,* and D.N. Smithe*			
7. PERFORMING ORGANIZATION NAME(S) AND ADDRESS(ES) Naval Research Laboratory Washington, DC 20375-5320			**8. PERFORMING ORGANIZATION REPORT NUMBER** NRL/FR/6840--95-9782
9. SPONSORING/MONITORING AGENCY NAME(S) AND ADDRESS(ES) Office of Naval Research Arlington, VA 22217			**10. SPONSORING/MONITORING AGENCY REPORT NUMBER**

11. SUPPLEMENTARY NOTES

*Mission Research Corporation, Newington, VA 22122

12a. DISTRIBUTION/AVAILABILITY STATEMENT Approved for public release; distribution unlimited.	12b. DISTRIBUTION CODE

13. ABSTRACT (Maximum 200 words)

Field emitter array structures are under consideration as the gated electron source in inductive-output amplifiers currently being designed, due to the potential for spatio-temporal modulation at the cathode surface. Emission gating of electron beams places stringent demands on the cathode structures where modulation occurs. In spite of the intense interest generated by these structures, a simple analytical treatment of their properties has not been forthcoming. In this work, we present a simplified theory of a gated FEA triode geometry, describe a numerically intensive calculation of current-voltage characteristics and other properties, and describe a semi-numerical model that combines the features of both. The semi-numerical model is being developed as a more comprehensive device analysis tool to predict RF amplifier performance in determining FEA properties that best meet IOA objectives.

14. SUBJECT TERMS			15. NUMBER OF PAGES
Field emission arrays Inductive output amplifiers Fowler-Nordheim	Simulation		58
			16. PRICE CODE

17. SECURITY CLASSIFICATION OF REPORT UNCLASSIFIED	18. SECURITY CLASSIFICATION OF THIS PAGE UNCLASSIFIED	19. SECURITY CLASSIFICATION OF ABSTRACT UNCLASSIFIED	20. LIMITATION OF ABSTRACT UL

NSN 7540-01-280-5500

CONTENTS

Accesion For

NTIS CRA&I	☑	
DTIC TAB	☐	
Unannounced	☐	
Justification		

By

Distribution /

Availability Codes

Dist	Avail and / or Special
A-1	

THEORY AND SIMULATION OF A GATED FIELD EMITTER: ANALYSIS AND INCORPORATION INTO MACROSCOPIC DEVICE CHARACTERIZATION

INTRODUCTION

Recent improvements in gated field emission array (FEA) technology provide a new alternative to thermionic electron beam sources [1] for emission gating at frequencies above ultra high frequency (UHF). This new opportunity, however, is subject to the integration of FEA technology into the vacuum tube environment. The principal advantages of microfabricated FEAs are the negligible tip-to-gate transit time and the high transconductance. FEA structures can modulate the beam density at high frequency and with good spatial localization, thereby making possible significant improvements in amplifier performance [2]. They have also been successfully used in the creation of flat panel displays [3] and other devices. Electrons from the ultra sharp tips (radius of curvature is on the order of 100 Å) can be emission modulated by applying an oscillating voltage to the gate that is coplanar with the emitter tips. FEAs, therefore, promise orders of magnitude improvement in frequency response over the thermionic cathodes (for which the gate plane is on the order of 20 μm from the cathode surface) due to limitations associated with transit time effects.

Because of this, considerable interest in developing an FEA cathode for inclusion into a twystrode or klystrode amplifier configuration has developed. Assumptions regarding the relation between the cathode current and the gate voltage are required to estimate inductive output amplifier (IOA) performance characteristics (e.g., gain, bandwidth, frequency of operation, efficiency) [4]. Consequently, the prediction of device performance has been impeded by the lack of a simple methodology for comparison of disparate FEA structures. Different fabrication methods produce widely different gate apertures, emitter heights, radii of curvature at the tip, and other geometric, as well as material, differences. The FEA unit cell, therefore, exhibits different current-voltage characteristics, transconductances, and capacitances.

Experimental data are well characterized by the Fowler-Nordheim (FN) equation [5,6], and modeling efforts typically take advantage of this. However, numerous physical effects mitigate against simple first-principles analysis of field emission from an FEA tip, and therefore invite the question "Is FEA performance predictable?" Effects such as the influence of the anode voltage during low current operation, or space charge effects during high current operation, may be amenable to a first-principles analysis, and a fundamental understanding of these effects seems possible. Other effects, well known to fabricators, include contamination, outgassing, seasoning, migration, dulling, and snapback. These are influenced by manufacturing, conditioning, and operational history, and are difficult to interpret in terms of first principles. Typically, these effects are controlled or held constant by holding to a strict operational regimen. Another effect that can prevent first-principles analysis of emission from an FEA tip is geometric irregularity of the tips. Recent transmission electron microscope (TEM) photographs indicate that actual tip shapes are highly irregular, whereas convenient analytical models assume spherical or elliptical shapes. Certain data support the notion of emission from a single, or perhaps a few, sites on a tip [7], in marked

contrast to the idea of emission occurring continuously over a broad area. Although the actual quantum-mechanical process may have a classical counterpart, key ingredients, such as the electronic charge, remain quantized. At scales of interest, only a single electron may exist in the vicinity of the gate, which may alter our understanding of "space charge" in depressing surface fields. "Turn on," in which a seemingly dysfunctional tip under some subtly changing influence suddenly begins to emit, has been observed, again suggesting lack of continuity. In light of this, it appears improbable that a truly predictive and comprehensive theory or simulation analysis can be found.

Statistical Models

Discrete: The Linear Distribution in B

But before such pessimism is accepted, the fact remains that the Fowler-Nordheim characterization of experimental data is of great utility, even though the fabrication, processing, and even measurement, procedures vary widely. We must therefore ascertain exactly what can be inferred from the experimental data through a statistical analysis. Let the individual tips in a field emission array (FEA) individually obey a Fowler-Nordheim relation (a similar analysis has been performed by Levine [8] at lower emissivities for flat displays). The ith tip is characterized by (the "*fn*" subscript on A and B is suppressed):

$$I_i(V) = A_i V_g^2 \exp\left(-B_i / V_g\right) , \tag{1}$$

where V_g is the gate voltage (below, the "g" subscript is suppressed). A plot of $\ln(I_i/V_g^2)$ vs $1/V_g$ is linear. Below, we refer to this as "Fowler-Nordheim (FN) behavior" (see Appendix A).

Assume that the number of tips characterized by B_i is n_i. Then the average current per tip from an FEA containing N tips is:

$$\langle I(V) \rangle = \frac{1}{N} \sum_{i=1}^{N} I_i(V) = \frac{1}{N} I_o(V) \sum_{i=1}^{N_B} n_i \frac{A_i}{A_o} \exp\left[(B_o - B_i) / V\right] , \tag{2}$$

where A_o and B_o remain to be specified, and where $\Sigma n_i = N$. Consider the case where the B's are linearly distributed according to $B_i = B_o + (i-1) \Delta B /(N_B-1)$, which we refer to as the "Linear Distribution." Further, assume that $n_i A_i \approx (N / N_B) A_o$. Because A_{fn} increases with tip radius (as does B_{fn}), this implies that a linear distribution in B's does not entail a uniform distribution in tip radius: n_i is larger for the sharper tips. Performing the summation in Eq. (2), <I> is given by

$$\langle I \rangle = \frac{1}{N_B} I_o(V) \frac{\left[1 - \exp\left(-\frac{N_B}{N_B-1} \frac{\Delta B}{V}\right)\right]}{\left[1 - \exp\left(-\frac{1}{N_B-1} \frac{\Delta B}{V}\right)\right]} . \tag{3}$$

As $N_B \to \infty$ (the continuum limit), $<I> \approx (V/\Delta B) I_o(V) [1-\exp(\Delta B/V)]$. The continuum limit may also be obtained directly by introducing the ("linear") distribution function $(n_i A_i / N A_o) \Rightarrow f(B) \, dB = dB$ $\theta(B - B_o) \, \theta(B_o + \Delta B - B)/\Delta B$, and transforming the summation in Eq. (2) into an integral. $f(B)$ is so defined that its integral over all B is unity.

For $\Delta B/V \ll 1$, we see that $\langle I \rangle \approx I_o(V)$, i.e., the tips are highly uniform. For $\Delta B/V$ sufficiently large (but small compared to N_B), $\langle I \rangle \approx (V / \Delta B) I_o(V)$. Strictly speaking, the coefficient $(V / \Delta B)$ will cause nonlinearities in an FN plot, but the question remains, to what extent are these non-linearities apparent? We return to this shortly.

Continuum

Consider the continuum extension of Eq. (2) for which the largest and smallest B_i's are denoted by B_+ and B_-, respectively. Let the distribution of B's be analogous to the Gaussian distribution:

$$f(B) = \frac{\exp\left[-(B - B_o)^2 / \sigma^2\right]}{\int_{B_-}^{B_+} \exp\left[-(B - B_o)^2 / \sigma^2\right] dB}.$$

(4)

Because $(B_+ - B_o)$ need not equal $(B_o - B_-)$, B_o will not in general correspond to the mean B nor will σ correspond to the standard deviation. At present, they are simply parameters specifying the distribution of B's. In what follows, we do not let $B_\pm$ go to $\pm \infty$ immediately. For example, consider the characteristics of the tips created by laser holography [12]: the radius of curvature is on the order of 10 to 50 Å. We expect, given the size of individual atoms, that B_- will likewise be constrained to this range, although B_+ need not be. Consequently, the distribution of B's for these tips is probably not a full Gaussian, and we therefore do not approximate the denominator of Eq. (4) by $\sqrt{\pi}\,\sigma$. Evaluating $\langle I \rangle = \int f(B) I(V) dB$ gives:

$$\langle I \rangle = I_o(V) \exp\left(\eta^2\right) \left[\frac{\mathrm{Erf}(x_+ + \eta) - \mathrm{Erf}(x_- + \eta)}{\mathrm{Erf}(x_+) - \mathrm{Erf}(x_-)}\right],$$

(5)

where $x_\pm = (B_\pm - B_o)/\sigma$ and $\eta = \sigma/(2V)$, and where $\mathrm{Erf}(x) = (2/\sqrt{\pi})\{\int_0^\infty \exp(-x^2) dx\}$ is the error function [11].

In the limit that $x_o = 0$ and $\Delta = (x_+ - x_-)/2$ approaches ∞, we find:

$$\langle I \rangle \approx I_o(V) \exp\left(\eta^2\right) \left[1 - \frac{4}{\sqrt{\pi}} \Delta \eta^2 \exp\left(-\Delta^2\right)\right],$$

(6)

which corresponds to the findings of Levine: FN-like behavior will occur only if σ is small, where σ is approximately the standard deviation. Physically, there is not a preponderance of tips with the smallest B-value; therefore, linearity in the FN behavior restricts the distribution of B values that may be present.

Second, consider the case where Δ is small by comparison to $x_o \pm \eta$ and x_o, approximating the linear distribution of B's encountered in Eq. (3) (note that x_o *need not equal* B_o/σ). It can be shown that

$$\langle I \rangle \approx I_o(V)\, e^{-2x_o\eta}.$$

(7)

The combination $2x_o\eta = (B_+ + B_- - 2B_o)/2V$; consequently, $\langle I \rangle/V^2 = \exp(-B_m/V)$, where $B_m = (B_+ + B_-)/2$, similar to the discussion following Eq. (3).

Finally, consider the case where $B_- = B_o$ and $B_+ = \infty$. This case resembles half of the Gaussian distribution (and is referred to as the "half-Gaussian" distribution). The current becomes

$$\langle I \rangle = I_o(V) \exp\left(\eta^2\right)\left[1 - \mathrm{Erf}(\eta)\right]$$

(8)

or η large, $1 - \mathrm{Erf}(\eta) \approx \exp(-\eta^2)/\eta\sqrt{\pi}$, and $<I> \approx (2V/\sigma)\, I_o(V)$. Again, a coefficient linear in V is obtained.

Least-Squares Fit of <I>: FN - Linearity of a Distribution of Emitters

Let us define $y = \ln(<I>/V^2)$ and $x = 1/V$ (which does not correspond to the x of the previous section). We desire to find the best polynomial approximation to y, we denote as y'. We define $x_o = (V_{max} + V_{min})/V_{max}V_{min}$, and similarly, $\delta = (V_{max} - V_{min})/V_{max}V_{min}$, where V_{max} and V_{min} denote the range over which we desire the best fit. The polynomial approximation of order n, which is the best least-squares approximation, can then be given by

$$y'(x) = \sum_{k=0}^{n} C_k \, P_k\!\left(\frac{x - x_o}{\delta}\right).$$

(8a)

$P_k(x)$ is the Legendre polynomial of degree k, and the C_k are determined by

$$C_k = \left(k + \tfrac{1}{2}\right) \int_{-1}^{1} y(x)\, P_k(z)\, dz$$

(8b)

where we have introduced $z = (x - x_o)/\delta$. The Error and Coefficient of Correlation are analogous to the equivalent formulae in Appendix A. For a best linear fit, we truncate the summation in Eq. (8a) at $n = 1$. As shown in Appendix A, the presence of V-dependent coefficients does alter the estimates of the best A_{fn} and B_{fn}. Consequently, the nature of the distribution of the emitters as a function of B_{fn} (or, equivalently, as a function of tip radius) can greatly affect the estimate of the array's A_{fn} and B_{fn} parameters, as compared to those parameters for a particular FEA unit cell. In general, *a distribution of emitters will tend to lower the estimate of A_{fn} and raise the estimate of B_{fn}* compared to the unit cell by an amount depending on the nature of the V-dependence of the coefficient of $I_o(V)$. The exact distribution of emitters for a given array of field emitters is not, in general, known. In the absence of tip-by-tip examination, it is difficult to estimate, thereby motivating our restriction of the cases of interest to those where an analytic solution is obtainable, namely, the linear and half-Gaussian distributions.

In the absence of a tip-by-tip examination of an FEA or scaling experiments, and the nature of the approximations used in a statistical analysis, the linearity of experimental data appears to support arguments that the tips are very uniform, or that emission is due to one kind of tip or protrusion. A statistical analysis coupled with a comprehensive modeling of the FEA unit cell offers some hope that analysis of FEA tips from a Fowler-Nordheim approach may offer practical understanding of some aspects of their operation, and that geometric irregularity, whether it exists or not, does not prevent such analyses. Certainly, the one-dimensional Fowler-Nordheim equation relating current density to field at the surface (with modification to account for three-dimensional effects) is to a large extent valid, and, as we argue and show below, does not preclude (experimental) linear total current vs gate voltage relations for an FEA. Considerable light may be shed on this subject through electron beam profile characterizations of individual or small numbers of tips; this is currently underway at NRL

[13]. Regardless of whether high uniformity or small tip domination is responsible, the approach developed here addresses either situation.

One final point to make is that, due to the behavior of the current density $J(F)$ with respect to field, the total current from a tip will be dominated by those regions in which the field is largest. Therefore, geometric detail and variations will tend to be obscured by the sites with the sharpest curvature. The fact that the $I(V)$ characteristics are dominated by the dependence on one parameter (V) suggests that a "peak field" is responsible for most of the emission, i.e., the emission appears to be independent of the precise field distribution. This observation is reinforced in subsequent derivations.

APPLICATION OF 1-D TRANSPORT EQUATIONS TO 3-D GEOMETRIES

The most widely used equation to model electron field emission is the Fowler-Nordheim equation. This relates current density J to applied field F according to the relation (Appendix B)

$$J_{FN}(F) = a_{fn}(F)\, F^2\, e^{-b_{fn}(F)/F}\ ,\tag{9}$$

where the field dependence of a_{fn} and b_{fn} is shown explicitly, and is due to the field dependence of the function $v(y)$ and $t(y)$ (Appendix B). (For convenience, the tables are grouped at the end of the text.) Implicitly assumed in Eq. (9) is the field emission potential barrier, with an image charge contribution of the form

$$V(x) = \chi - F\,x - \frac{Q}{x}\ ,\tag{10}$$

where $\chi = \phi + \mu$ in the case of metals, or the electron affinity in the case of semiconductors. The use of the (Q/x) form of the image charge presupposes emission from a planar surface. In reality, surface curvature affects the form of the image charge contribution [14-16], and a careful derivation shows that the form of the denominator should be $(x + x_o)$ rather than merely (x) [17,18]. Furthermore, the form of Eq. (9) requires modification for semiconductors [19], although for present purposes we assume metallic parameters.

Its limitations notwithstanding, Eq. (9) is often applied to field emission from multidimensional structures. This is done by making the simple replacements $I = bJ$ and $F = \beta V_g$ (a procedure that has been roundly criticized [15,20], but nevertheless widely used) to "derive" current voltage relations amenable to experimental interpretation of data of the form

$$I(V_g) = A_{fn} V_g^2 e^{-B_{fn}/V_g}\ ,\tag{11}$$

where A_{fn} and B_{fn} are assumed to be constant. Two difficulties. First, the form of Eq. (9) does not ensure that A_{fn} and B_{fn} are even constant with respect to V_g. Other curves are also linear, to a good approximation, on an FN plot (Appendix A). Second, A_{fn} and B_{fn} are experimental parameters obtained from the fitting of data; they cannot be fundamentally derived using Eqs. (9) and (10) (especially in the absence of a statistical analysis) due to the ad hoc nature of (b) and (β): the problem of "measuring" J and F has simply been deferred to "measuring" b and β. Nevertheless, the comparison of FEA tips and geometries requires some figure of merit, and as will be shown, the FN A and B parameters extrapolated from the portion of the $I(V_g)$ curve where the device is intended to

operate serves that purpose. Consequently, there is a pressing need to make some analytical or simulation-based estimation of A_{fn} and B_{fn}. In the past, they have been estimated by using finite-element methods or other techniques [20-24]. But this is computationally intensive and does not transparently reveal the parametric dependence of, for example, the $I(V)$ relations, on geometry and materials. This report provides a simple analytical model (Saturn) , explores its limitations, compares it with a full numerical model based on the boundary element method [25,26], and proposes a semi-numerical model that endeavors to overcome the limitations of the Saturn model, but nevertheless is computationally far less intensive than the boundary element model. The analytical techniques used by the Saturn model borrow heavily from earlier analytical work dealing with field emission tips in a diode configuration [27].

The simple, or Saturn, model, replaces the field emission tip with a sphere and the gate with a charged ring. An analytic relation then exists between the gate radius and voltage, the sphere radius, the field, and its angular variation on the sphere, from which the total emitted current can be derived analytically. For reasons to be discussed, the estimation of gate voltage is problematic in this model, but the utility of the model lies more in its ability to makes qualitative predictions that are borne out in the boundary element treatment, rather than as a precise computational tool. Finally, the methodology used in the simple model motivates the approximations made in the semi-numerical approach. The boundary element method models the tip, gate, and anode surfaces with charged ribbons. At present, attention is restricted to electrodes with azimuthal symmetry. The charge on each ribbon is determined by a matrix solution of Poisson's equation for a given tip, gate, and anode potential. The field and area of each ribbon is then calculated, from which the current per ribbon can be obtained by using Eq. (1). The semi-numerical model combines the analytic approach of the Saturn model with minimal input from the boundary element model, thereby using analytic current vs gate voltage formulae from the Saturn $I(V)$ model. The angle-dependent field along the surface provided by a geometric parameterization table constructed from the boundary element method. The resulting simulation tool is then in a position to rapidly form estimations of A_{fn} and B_{fn}, as well as other parameters (such as capacitance) needed in a full-scale simulation of total inductive output amplifier (IOA) device performance. The full-scale device simulation is a program of considerable activity in the FEA-RF Amplifier program at NRL because of its utility in relating device performance to tip parameters to affect the selection process for FEAs fabricated by widely different techniques [4].

FIGURES OF MERIT AND THE FEA UNIT CELL

Before delving into the theory and simulation of the unit cell, the practical objectives should be identified. The performance required of an FEA cathode derives from the specifications of the amplifier for which it is intended. In the case of an inductive output amplifier, which requires a high-frequency gated cathode, knowledge of the $I(V)$ characteristic curve and the equivalent circuit of a unit cell is sufficient to predict the FEA's effect on the performance of the amplifier. Moreover, the critical information is conveyed by just four parameters: A_{fn} and B_{fn}, the maximum available current per tip, i_{pk}, and the net gate-to-base capacitance per unit cell (C). General guidance for optimizing these parameters can be obtained simply by minimizing the drive power required to gate the beam.

The transconductance of a voltage-controlled current source is defined as the derivative of beam current with gate potential, i.e., $g_m = \partial I_{\text{beam}}/\partial V_g$. To relate FEA performance to amplifier gain, a power transconductance is defined as the incremental current for an increment in drive power: $g_P = \partial I_{\text{beam}}/\partial P_{dr}$ (in units of amperes per watt). In a gated FEA cathode, the gate and the emitting surface form a largely capacitive load on the input circuit; the power required for a voltage swing V_{rf} on the

gate is just $P_c = (^1/_{2Q})\omega C V_{rf}^2$, where C is the capacitance of the array, and the voltage swing V_{rf} is defined by $V_g = V_{dc} + V_{rf}\sin(\omega t)$, in which ω is the drive frequency. Consequently,

$$g_P \equiv \frac{\partial\, i_b}{\partial P_{dr}} = g_m \frac{2\,Q}{\omega_o\,C V_{rf}}, \tag{12a}$$

where Q is the quality factor of the input circuit and ω_o is the resonance frequency of the input circuit. (A perfect and lossless impedance match is presumed.) We proceed by calculating g_m at the maximum of the emission; this is the most reasonable approximation for strongly modulated beams because the input power requirement is driven by the need to reach that maximum emission. By assuming that I_{beam} is given by Eq. (11) and letting the peak value of I_{beam} and V_g be denoted by I_{pk} and V_{pk}, respectively, we obtain

$$g_P = \frac{I_{avg}}{\left(I_{avg}/I_{pk}\right)}\frac{2\,V_{pk} + B_{fn}}{V_{pk}^2} \bullet \frac{2\,Q}{V_{rf}\omega_o\left(C_{add} + N_{tips}C_{tip}\right)} \tag{12b}$$

where N_{tips} is the total number of unit cells, and C_{add} is capacitance of the FEA over and above the sum over the unit cells. The rf voltage V_{rf} can be obtained in terms of the modulation current ratio I_{avg}/I_{pk}, by convoluting of the gate voltage signal on Eq. (11). For $I_{avg}/I_{pk} < 0.4$, the result is:

$$V_{rf} = \frac{1}{2\pi\left(I_{avg}/I_{pk}\right)^2}\left(\frac{V_{pk}^2}{2\,V_{pk} + B_{fn}}\right) \tag{12c}$$

yielding finally:

$$g_P = \frac{4\pi\,Q\,A_{fn}\exp\left(-B_{fn}/V_{pk}\right)}{\omega_0\left(\dfrac{C_{add}}{N_{tips}} + C_{tip}\right)}\left(I_{avg}/I_{pk}\right)^2\left(2 + \frac{B_{fn}}{V_{pk}}\right)^2. \tag{13}$$

This relation offers several hints for the optimization of FEAs for maximum gain. The $I(V)$ characteristic curve and the capacitance are the FEA characteristics that appear here; in other words, the FEA is effectively described by A_{fn}, B_{fn}, and C, with the operating point given either by i_{pk} or V_{pk}. The power transconductance is most sensitive to the exponential implicit in Eq. (11), and reducing B_{fn} is the most effective means of improving the FEA. The two parameters A_{fn} and C occur only as the ratio A_{fn}/C; they can be traded-off against each other. This useful figure of merit for the emission gating assembly correlates closely to the gain of the amplifier.

ANALYTIC EVALUATION OF CURRENT VS GATE VOLTAGE AND FEA PARAMETERS

The analytical dependence of A_{fn} and B_{fn} on material and geometric parameters for simple geometries must be determined. (The technique is extensible to more complicated surfaces, but this is deferred to a future work.) The dependencies rely on the model of the triode geometry (elliptical, hyperbolic, sphere on post); in this section, we concentrate on features common to all models.

Extraction of $I(V)$ from $J(F)$

The total current from an arbitrarily shaped emitter surface is given by

$$I(V_g) = \int_S \vec{J} \cdot d\vec{S},$$ (14)

where $\vec{J}$ is the current density and $d\vec{S}$ is the differential surface area. A widely used method [20-23] of estimating total current from a tip is to approximate the component of the current density $\vec{J}$ normal to the surface by the 1-dimensional Fowler-Nordheim $J(F)$ as given in Eq. (9) with the approximations for $v(y)$ and $t(y)$ as given in Table 1. We are more careful than that here, in that we calculate $v(y)$ and $t(y)$ exactly.

If we further assume rotational symmetry (the cylindrical coordinates will therefore be designated by (ρ, z)) about the $\vec{z}$ axis, then we have

$$I(V_g) = 2\pi \int_0^{a_e} \sqrt{1 + \left(\frac{\partial z_e}{\partial \rho}\right)^2}\, J[F(\rho)]\, d\rho,$$ (15a)

where $z_e(\rho)$ describes the surface of the emitter. For an elliptical emitter (which serves as a generic tip configuration in that it can be matched to different models) characterized by $\rho = a_e \sin(\theta)$ and $z = R\, a_e \cos(\theta)$, where a_e is the base radius of the emitter, this becomes

$$I(V_g) = 2\pi\, a_e^2 \int_0^1 \sqrt{R^2(1 - x^2) + x^2}\, J[F(x)]\, dx,$$ (15b)

where $x = \cos(\theta)$ [27]. Hyperbolic and sphere on cone models result in analogous formulae.

Extension of the FN Equation to Semiconductor or Metallic Multidimensional Tips

Three complications arise in the treatment of real emitters:

• Equation (9) as given ignores temperature and variations in chemical potential, which can lead to errors when applied to semiconductors (although not for metals).

• For semiconductors, or for metals treated with, e.g., cesium, the barrier height experienced by the tunneling electrons may be so low at high fields that the Fowler-Nordheim equation is no longer appropriate.

• Curvature of the emitter surface alters the form of the image charge from Q/x to something that is geometry-dependent.

• Actual tips have bumps or protrusions; in the case of semiconductor tips, the geometry can be pyramidal rather than conical, generating a field-enhancement effect along the pyramid edge.

For the first two, modified Fowler-Nordheim equations can be found for both metallic and semiconductor parameters [19], but for low barrier heights, a different approach toward quantum

Table 1 — Constants and Parameters

Symbol	Meaning	Value / Equation	Units
Units			
Å	angstroms	10^{-10}	meters
eV	electron volts	1.6×10^{-19}	Joules
fs	femtoseconds	10^{-15}	seconds
e	unit charge	1.6×10^{-19}	Coulombs
$e/(fs\,\text{Å}^2)$	current	1.6×10^{12}	amps/cm^2
Fundamental Constants			
c	velocity of light	2998.79	Å/fs
α	fine structure constant	1/137.04	-
$\hbar$	Plank's constant / 2π	0.658028	eV fs
mo	electron rest mass	511000	eV/c2
ao	Bohr radius	0.529	Å
R_y	Rydberg energy	13.606	eV
ε_o	permittivity of free space $= e^2/4\pi\alpha\hbar c$	1/180.95	eV Å
Statistical Models			
A_i	FN parameter of *i*th emitter	-	μA/V^2
B_i	FN parameter of *i*th emitter	-	volts
<I>	average current per tip	-	μA
N	number of emitters	-	-
N_B	number of different B values	-	-
n_i	number of emitters with $B = B_i$	-	-
σ	Gaussian distribution parameter	-	volts
B_o	reference B value	-	volts
$x_{\pm}$	scaled maximum / minimum B value	$(B_{\pm} - B_o)/\sigma$	-
x_o	scaled reference B value	$(x_+ + x_-)/2$	-
Δ	scaled spread	$(x_+ - x_-)/2$	-
η	scaled Gaussian distrib. parameter	$\sigma/(2V)$	-
$P_k(z)$	Legendre polynomial	-	-
C_k	Legendre polynomial coefficient	-	-

Table 1 (Continues) — Constants and Parameters

Fowler-Nordheim Terms

J_{FN}	Fowler-Nordheim current density	$a_{fn} \, F^2 \, exp(-b_{fn}/F)$	Amps/cm^2
a_{fn}	$J_{FN}(F)$ parameter (F dependent)	$\dfrac{N_c}{16 \, \pi^2 \hbar \phi t(y)^2}$	Amps/cm^2
b_{fn}	$J_{FN}(F)$ parameter (F dependent)	$\dfrac{4}{3}\left(\dfrac{2m\phi^3}{\hbar^2}\right)^{1/2} v(y)$	eV/Å
$v(y)$	function, approximated by quadratic	$\approx v_o - y^2$	-
v_o	constant	≈ 0.93685	-
$t(y)$	function, approximated by constant	≈ 1.05657	-
F	field	-	eV/Å
ϕ	work function (metal)	-	eV
μ	chemical potential or Fermi level (metal)	-	eV
χ	electron affinity (semiconductor)	-	eV
y	Fowler-Nordheim variable	$\sqrt{(4QF)/\phi}$	-
Q	planar image charge coefficient	$\dfrac{\alpha \hbar c}{4} \dfrac{K_s - 1}{K_s + 1}$	eV Å
K_s	dielectric constant	∞ for metals	-
N_c	conversion factor	1.6×10^{12}	(amps/cm^2) $\times$ (e/Å^2 fs)$^{-1}$

FEA Device and Geometrical Factors

$I(V_g)$	current from unit cell	$A_{fn} \, V_g^2 \, exp[-B_{fn}/V_g]$	amps
A_{fn}	FN current parameter (constant)	-	amps/cm^2
B_{fn}	current parameter (constant)	-	volts
V_g	gate voltage	-	volts
V_a	anode voltage	-	volts
F_{tip}	field at apex of tip	$F(a_s,0)$	eV/Å
λ	field variation factor	-	-
$a(\theta)$	radius of curvature along emitter	-	Å
b	area factor	$I(V_g) / J(F_{tip})$	cm^2
β	inverse temperature	$11604.5/T$	1/eV
T	temperature	-	Kelvin
β_f	field enhancement factor	-	1/Å
C	capacitance	-	Coul/volts
I_p	peak current	-	amps
I_{ave}	average current	-	amps

Table 1 (Continues) — Constants and Parameters

Saturn Model

F_a	field coefficient due to anode	V_a / z_a	eV/Å
F_g	field coefficient due to gate	$Q_g / r_g a_s$	eV/Å
Q_g	charge on equivalent gate ring	-	eV Å
r	spherical coordinate	-	Å
θ	spherical coordinate	-	radians
ρ	cylindrical coordinate	$r \cos\theta$	Å
z	cylindrical coordinate	$r \sin\theta$	Å
a_g	radius of gate	-	Å
a_r	radius of ring of charge	-	Å
r_g	radial sphere to ring separation	$\sqrt{z_g^2 + a_r^2}$	Å
r'_g	radial sphere to gate separation	$\sqrt{z_g^2 + a_g^2}$	Å
$\cos(\alpha)$	ring angle	z_g/r_g	
t	"thickness" of gate	$a_r - a_g$	Å
a_s	radius of equivalent sphere	-	Å
z_g	distance from equivalent sphere to gate plane	-	Å
z_a	distance from equivalent sphere to anode	-	Å
$K(p)$	complete elliptical integral of 1st kind	$\displaystyle\int_0^{\pi/2} \frac{dx}{\sqrt{1 - p^2 \sin^2(x)}}$	-
p	K(p) parameter	$(4\rho\rho')^{1/2} / \gamma$	-
γ	ring potential parameter	$[(\rho+\rho')^2 + (z-z')^2]^{1/2}$	Å

transport may have to be used (Appendix B). With regard to the image charge, the field F and the barrier height χ can be altered by small quantities, dependent on the radius of curvature of the emitter at the location where the current density J is being evaluated [27, 28]. To a very good approximation, χ and F can be replaced by the quantities F_a and χ_a in the (modified) Fowler-Nordheim equation, where

$$\chi_a(\theta) = \chi + \frac{Q}{2\,a(\theta)}$$
$$F_a(\theta) = F(\theta) + \frac{Q}{\left[2\,a(\theta)\right]^2} , \qquad (16)$$

so that the barrier potential resembles $\chi_a(\theta) - F_a(\theta)\,x - Q/x$. In the models considered here, the emitter tip is approximated by a sphere, so that $a(\theta) \approx a_{\text{sphere}}$ for the values of θ where $J(F(\theta))$ is significant. Finally, with regard to surface curvature, the bumps and protrusions *on axis* have the dominant effect. Ridges, being a protrusion in a two-dimensional space, have less field enhancement than bumps in a three-dimensional space, and therefore, pyramidal complications are not immediately of concern (Appendix C).

Fowler-Nordheim Parametrization of $I(V_g)$ and Area Factor

In pursuit of an analytic $I(V_g)$, two assumptions are expeditious: Assume that the current density can be approximated by Eq. (9), (note that this does *not* imply a simple correspondence with Eq. (11), as $v(y)$ and $t(y)$ are, in general, field-dependent). Also assume, at least for small θ, the field to be approximated by

$$F(\theta) = \frac{F_{tip}}{1 + \lambda\left(1 - \cos(\theta)\right)} , \qquad (17)$$

where F_{tip} = field on-axis and λ characterizes the falloff of field along the equivalent sphere representing the surface, both of which are gate-voltage dependent. Inserting these approximations into Eq. (15b) gives

$$I(V_g) \approx 2\pi\,a_e^2\,J_{\text{FN}}(F_{tip}) \int_0^1 \frac{\sqrt{R^2 - (R^2 - 1)(1 - y)^2}}{\left(1 + \lambda y\right)^2} \exp\left(-\frac{b_{fn}(0)}{F_{tip}}\lambda\,y\right) dy , \qquad (18)$$

where $y = 1-\cos(\theta)$ and a_e is the base radius of the elliptical emitter. The coefficient of $J_{\text{FN}}(F_{tip})$ is the area factor (*b*). Finally, F_{tip}, λ, C, β, and the peak and average currents I_p and I_{ave} are dependent on the geometrical factors, and are, therefore, dependent on the model of the triode we adopt. This is taken up next.
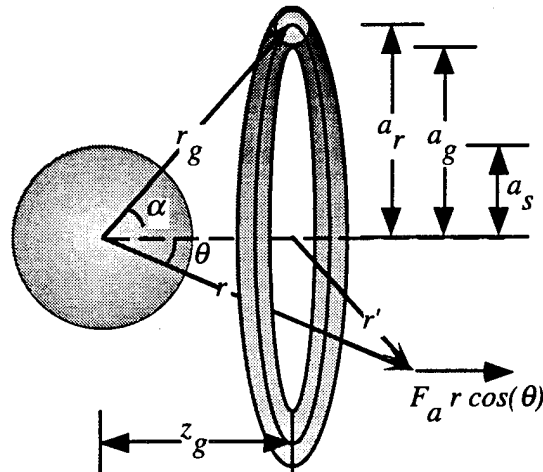
THE SATURN MODEL

Potential Distribution of Sphere and Ring, and the Electric Field

In some sense, the simplest model of an ungated field emitter (diode) is given by the "floating sphere" model [24, 29], in which a sphere whose radius is equal to the tip radius of the field emitter

is suspended between parallel plates. The simplest modification to this model, which endeavors to approximate a triode, is to insert a ring of charge (not necessarily coplanar) somewhere along the symmetry axis. We further replace the parallel plates by a background field of the form $-Fz$. Let the origin of the coordinate system be centered on the sphere approximating the tip (Fig. 1). The potential anywhere is therefore the sum of three components — the anode, the gate ring (or simply *gate*), and the sphere.

Fig. 1 —Saturn model, showing relevant parameters

For the anode, the potential is given by

$$\phi_a = - F_a \, r \cos (\theta) \,, \tag{19}$$

where we let $F_a = V_a/z_a$, where V_a is the potential of the anode and z_a is the distance from the center of the sphere to the anode plane. The justification for this assignment goes back to the diode calculations in which an analogous expression was found on axis [27]. Analogously, and using the nomenclature introduced in Fig. 1 and Table 1, we define the gate potential to be

$$\phi_g = \frac{Q_g}{2\pi} \int_0^{2\pi} d\varphi \left[\rho^2 + (z - z_g)^2 + a_r^2 - 2\, \rho\, a_r \cos(\varphi) \right]^{-1/2}$$

$$= \frac{2}{\pi} Q_g \frac{K(p)}{\gamma} \tag{20a}$$

$$= \frac{Q_g}{r_g} \sum_{l=0}^{\infty} \left(\frac{r}{r_g} \right)^l P_l\big(\cos (\alpha)\big) \, P_l\big(\cos (\theta)\big) \,,$$

where we have introduced the integral definition, the complete elliptical integral $K(p)$, and the Legendre polynomial expansion for $r < r_g$. The value for Q_g is, as yet, unspecified; note that it implicitly includes a factor of $(1/4\pi\varepsilon_o)$. $K(p)$ is defined as

$$K(p) = \int_0^{\pi/2} \frac{dx}{\sqrt{1 - p^2 \sin^2 x}} \ . \tag{20b}$$

Finally, for the tip, the potential is given by

$$\phi_s = \sum_{l=0}^{\infty} A_l \, r^{-(l+1)} P_l\big(\cos(\theta)\big) , \tag{21}$$

where the A_l's are to be determined.

Determination of the Legendre Coefficients, Gate Charge, and Field on the Sphere

On the surface of the sphere, the potential $\phi = \phi_a + \phi_g + \phi_s$ vanishes. This serves to specify the A_l's:

$$A_l = -\frac{Q_g}{r_g}\left(\frac{a_s}{r}\right)^{(l+1)}\left(\frac{a_s}{r_g}\right)^l P_l\big(\cos(\alpha)\big) - F_a \frac{a_s^3}{r^2}\delta_{l1} \ , \tag{22}$$

where $\delta_{ll'}$ is the Kronecker delta function. Next, around the gate ring, the equipotential lines are approximately toroidal. Let a point separated from the gate ring by a distance $t = a_r - a_g$ be at the potential V_g. Assuming t is not large compared to other parameters, it can be taken as half of the gate thickness (this approximation is poor for typical FEAs since the gate thickness is not in general small by comparison to other terms). Then Q_g is determined by

$$V_g = \frac{2}{\pi} Q_g \frac{K(p_o)}{\gamma_o} + F_a z_g \left[1 - \left(\frac{a_s}{r'_g}\right)^3\right] - \frac{Q_g}{r_g} \sum_{l=0}^{\infty} \left(\frac{a_s}{r'_g}\right)^{l+1} \left(\frac{a_s}{r_g}\right)^l P_l\!\left(\frac{z_g}{r_g}\right) P_l\!\left(\frac{z_g}{r'_g}\right) . \tag{23a}$$

Note that $r'_g = \sqrt{(z_g^2 + a_g^2)} \neq \sqrt{(z_g^2 + a_r^2)} = r_g$. For $a_s \ll a_g$, only the first term of the summation need be retained, and we have the approximation

$$Q_g \approx \frac{\left(V_g - F_a z_g\right)}{\dfrac{2\,K(p_o)}{\pi\,\gamma_o} - \dfrac{a_s}{r_g\,r'_g}} \ , \tag{23b}$$

where p_o and γ_o are p and γ evaluated at $\rho = a_g$ and $z = z_g$, respectively. The charge on the sphere is given by A_l for $l = 0$, or $Q_s = Q_g \, a_s / r_g$. As expected, this result is analogous to the image charge solution to the problem of a conducting sphere under the influence a point charge [30].

Along the surface of the sphere, the force ($F = -eE$) on the electrons points radially outward. We can therefore calculate the field along the sphere by taking the radial derivative of ϕ and evaluating it at $r = a_s$. Doing so yields

$$F(a_s,\theta) \equiv - F(\theta)$$

$$= -3\, F_a \cos{(\theta)} - F_g \sum_{l=0}^{\infty} (2l+1) \left(\frac{a_s}{r_g}\right)^{l} P_l\Big(\cos{(\alpha)}\Big) P_l\Big(\cos{(\theta)}\Big) , \tag{24}$$

where we have introduced $F_g = Q_g/(r_g a_s)$. As it should, Eq. (24) naturally separates into a cathode and anode part. In general, $F_{tip} \neq \beta\, V_g$ but is something more complicated. For a distant anode generating a relatively weak F_a, the approximation acquires merit. The field at the tip ($\theta = 0°$) can be found by replacing $P_l(\cos(\theta))$ with (1) in Eq. (24). Again, if we assume that the sphere radius is much smaller than the gate radius, then we can approximate the λ factor by

$$\lambda_s \approx 3\left(F_a + F_g \frac{a_s z_g}{r_g^2}\right)\left[F_g + 3\left(F_a + F_g \frac{a_s z_g}{r_g^2}\right)\right]^{-1} = \frac{(F_{tip} - F_g)}{F_{tip}} , \tag{25}$$

where the s subscript on λ refers to Saturn. One consequence of Eq. (24) is that the field is not maximized for the tip of the emitter lining up with the gate plane. The emitter should be below (or above) the gate plane ($z_g > a_s$) by an amount that maximizes F as a function of z_g. This has been previously noted in numerical experiments [20]. Finally, note that λ_s will be small if the quantity $(a_s z_g/r_g^2)$ is small, as will happen in practice when real FEAs are considered for which the numerator is vanishing by comparison to the denominator.

Current and Capacitance in the Saturn Model

For the Saturn model, $R = 1$, for which Eq. (18) reduces to (dropping the s on λ):

$$I(V_g) = 2\pi\, a_s^2\, J_{\mathrm{FN}}(F_{tip}) \int_0^1 \frac{1}{(1 + \lambda y)^2} \exp\left(- \frac{b_{fn}(0)}{F_{tip}}\, \lambda\, y\right) dy, \tag{26}$$

where $b_{fn}(0)$ is b_{fn} evaluated at $F = 0$. A good approximation to $I(V_g)$ is then given by

$$I(V_g) \approx \frac{2\pi\, a_s^2}{\lambda}\, F_2\left(\lambda, \frac{b_{fn}(0)}{F_{tip}}\right) J_{\mathrm{FN}}(F_{tip}) , \tag{27a}$$

where $F_n(\lambda, x)$ is given by [27]:

$$F_n(\lambda, x) = \int_0^{\lambda} (1 + y)^{-n}\, e^{-xy}\, dy . \tag{27b}$$

$F_2(\lambda, x)$ is bounded from below by $1/x$ (small field limit) and from above by $\lambda/(1+\lambda)$ (large field limit). For small fields at the tip, we therefore see that, in contradiction to the current density J, for the current I, $\ln(I/F^3)$ is approximately linear in $1/F$. The coefficient of $J_{FN}(F)$ in Eq. (27a) is typically referred to as the "area factor."

The capacitance in the Saturn model is given by the ratio of the charge on the sphere Q_s and the gate voltage V_g, which is related to the charge on the ring by the A_o term in the Legendre expansion.

The charge on the ring is given by Eq. (23b). An analytic expression exists for the sphere-to-gate capacitance that can be found in a manner analogous to that used for the boundary element model (described below). We note here that, depending on the geometry, Eq. (27) and the expression for C, may or may not be adequately approximated by the Saturn model.

Two points worth mentioning regarding Eq. (27). First, Eq. (27a) owes its simple form to the approximation $v(y) \approx v_o - y^2$ used in Eq. (26). Two problems are that $v(y)$ is not linear in F_{tip}, nor is $v_o - y^2$ the best (least-squares) approximation to $v(y)$ (Appendix B). The former problem is resolved by noting that for field values of interest, a linear approximation to $v(y)$ in the field is a reasonable approximation. For the latter, $v(y)$ may always be Taylor expanded about a (typical) field of interest in order to generate $v(y) \approx v'_o - v_1 y^2$, thereby entailing a minor modification to Eq. (27a). Second, $J_{FN}(F_{tip})$ in Eq. (27a) can be replaced by any other (superior) quantum transport model, e.g., one based on the Airy function solution to Schrödinger's equation [33]. This is particularly important if the work function becomes so low that at high fields, the Fowler-Nordheim equation is no longer a good approximation to $J(F)$. We consider a case of this below when the experimental data from MIT-Lincoln Labs are discussed.

Deficiencies of the Saturn Model

For a given F_{tip} and λ, we have found that the Saturn model, i.e., Eq. (27), is a good approximation to Eq. (26). The problem with the Saturn model lies with its estimate of F_{tip}, which ultimately depends on the estimate of Q_g, and also its estimation of λ. Although it is true that the charge density spikes near an edge [30] giving the justification for replacing the gate (a sheet of charge with a hole excised from it) with a ring of charge in the proximity of the edge of the hole, the remainder of the gate (and the charges on it) cannot be neglected. Consequently, for a given F_{tip}, the Saturn model tends to overestimate the value of V_g associated with it, as the result of to its neglect of the remainder of the gate compared to a full numerical solution. Attempting to correct this limitation results in the addition of more rings of greater radii with different Q's, but this is too similar to the actual numerical solution to merit elaboration. In summary, once a (correct) estimate between F_{tip} and V_g is established, the remainder of the machinery adopted for the Saturn model can be used to estimate current and related quantities.

THE BOUNDARY ELEMENT MODEL

Geometry, Parameters, and Implementation

A model that corresponds well to the actual geometry of the gated field emitter is expected to provide a more accurate comparison with the experimentally measured quantities. The axially symmetric unit cell model selected consists of an anode, a gate with hole, and a base plane with an emitter tip protruding (Fig. 2). This model is representative of several of the "vertical emitter" structures currently being considered in the FEA-based RF Amplifier Program at NRL. The small sizes characteristic of the apex of the emitter tips in comparison to the size and distances of the other electrodes suggest the use of a nonuniform discretization of the computational domain. The use of typical finite-difference formulations with uniform mesh is therefore contraindicated (as in SIMION and EGUN simulations). A variable-mesh finite-difference or finite-element technique could be used [21-23]. However, because the principal item of interest is the emission at the boundary, particularly in the small region near the emitter tip, a boundary-element model was chosen.
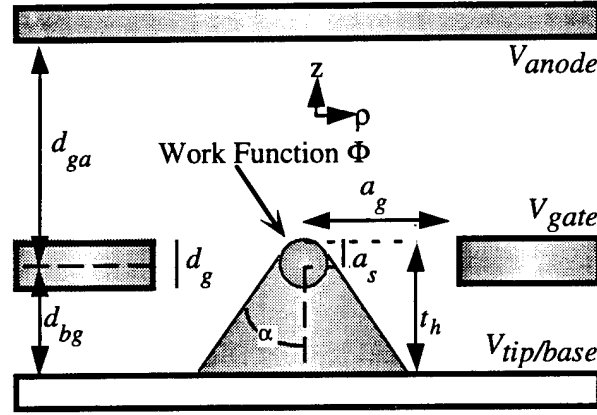
Fig. 2 — Generic FEA unit cell, showing relevant parameters

The boundary element technique [24] discretizes the boundary into sections (in our model, annular ribbons). These sections are taken to be quite small in the vicinity of edges and corners and increase in size (quadratically, in the example to be shown later) in the smooth boundary areas. The list of boundary elements and their physical attributes is developed from a parameterization suggested by experimentally pertinent quantities. These qualities include work function, potential, tip radius, tip height, gate hole radius, base-gate distance, gate-anode distance, gate thickness, and type of tip (sphere on cone, ellipsoid, tip on post, post height). A graphical user interface allows a rapid analysis of the system because of integration of the boundary element generator, potential solver, semi-numerical post-processor, and plotting package. After the geometry is specified, the time taken by the program package to extract the Fowler-Nordheim A_{fn} and B_{fn}, as well as C_{FEA}, parameters is less than a minute on a desktop computer.

Calculation of the Potential

The potential anywhere can be calculated by integrating over the surface charge densities on electrodes:

$$\phi(\vec{r}) = \frac{1}{4\pi\varepsilon_o} \int_\Omega \frac{\sigma(\vec{r}')}{\left|\vec{r} - \vec{r}'\right|} d\Omega \; , \tag{28a}$$

where $d\Omega$ is the differential surface element. Consider the approximation in which the conducting boundaries are broken up into ribbons of charge, each with a constant surface charge density [25]. This tends to lead to a faster numerical solution than assuming that the surface charge density has a linear dependence [26] and reflects our eventual intent to rely on a hybrid between the Saturn model and the boundary element model. Consequently, Eq. (28a) assumes the discretized form:

$$\phi(\rho,z) = \frac{1}{4\pi\varepsilon_o} \sum_{i=1}^N 4\sqrt{1 + s_{i+1/2}^2}\; \sigma_{i+1/2} \int_{\rho_i}^{\rho_i + \varepsilon_i} \rho' \frac{K(p)}{\gamma} d\rho' \; , \tag{28b}$$

where $s_{i+1/2} = (z_{i+1} - z_i)/(\rho_{i+1} - \rho_i)$, $\sigma_{i+1/2}$ is the charge density on the ith ribbon, $p = \sqrt{(4\rho\rho')}/\gamma$ and $\gamma = \sqrt{[(\rho+\rho')^2 + (z-z')^2]}$. The ρ_i are quadratically spaced, so that the ribbons are thinner near the axis of symmetry or near a conductor edge.

At the midpoint of each ribbon, ϕ is specified by the potential of the conducting surface. There are N ribbons, and we therefore have N values of ϕ denoted by $[\phi]_i \equiv \phi(\rho_{i+1/2}, z_{i+1/2})$, where ϕ is an N-component vector, $\rho_{i+1/2} = \rho_i + \varepsilon_i/2$, $z_{i+1/2} = z_i + s_{i+1/2}\varepsilon_i/2$, and $\varepsilon_i = (\rho_{i+1} - \rho_i)$. We can therefore rewrite Eq. (28b) as (where, analogous to the potential vector, $[\sigma]_i = \sigma_{i+1/2}$)

$$\vec{\phi} = \overline{\overline{M}} \cdot \vec{\sigma}$$

$$[\overline{\overline{M}}]_{i,j} = \frac{1}{\pi\varepsilon_o} \sqrt{1 + s_{j+1/2}^2} \int_{\rho_j}^{\rho_{j+1}} \rho' \, \frac{K(p)}{\gamma} \, d\rho' \, ,$$

(29)

where ρ_i and z_i are implicit in the definition of p and γ. The ϕ-vector is a known quantity (it is the value of the voltage segments on the tip, gate, and anode), and $M_{i,j}$ can be calculated. Eq. (29) can then be inverted to give the values of the charge densities on each ribbon: $\sigma = \overline{M}^{-1} \cdot \phi$. An advantage of this formulation is that $\overline{M}$ need be calculated only once (being geometry, and not potential, dependent) and inverted once (using, for example, LU decomposition); thereafter, for a different voltage on the gate and anode, only the ϕ vector needs to be altered to obtain a new σ.

The integral in Eq. (29) is generally evaluated by using a 4-point Gaussian quadrature routine, except when $|i-j| \leq 3$, in which case a 10-point Gaussian quadrature routine is used. The ring potential of Eq. (20a) can be derived from Eq. (28) by evaluating the integrand at the midpoint. When $i = j$, $K(p)$ contains a logarithmic singularity of the form $(1/2) \ln[16/(1-p^2)]$ as p approaches 1. The singular portion of the integrand can be analytically integrated. Dropping the $(i+1/2)$ subscript on (s) and (ρ) and the (i) subscript on (ε) on the right-hand side, we have:

(30)

$$\int_{\rho_i}^{\rho_{i+1}} \frac{\rho'}{\gamma} \frac{1}{2} \ln\left(\frac{16}{1-p^2}\right) d\rho' = \frac{\varepsilon}{288\rho^2}\left(\frac{1}{4}[96\rho^2 - (s^2+2)\varepsilon^2]\left[3\ln\left(\frac{256\,\rho^2}{(s^2+1)\varepsilon^2}\right) + 2\right] + 96\rho^2\right) .$$

The remainder, i.e., $\rho' \{K(p) - (1/2) \ln[16/(1-p^2)]\}/\gamma$, can be integrated by Gaussian quadrature.

Once the surface charge densities $\sigma_{i+1/2}$ are found by inverting the matrix equation (Eq. (29)), the field at the surface F_i and (normalized) charge per ribbon Q_i can be evaluated:

$$F_i \equiv \frac{\sigma_{i+1/2}}{\varepsilon_o}$$

(31)

and

$$Q_i \equiv \frac{1}{2\varepsilon_o} \sigma_{i+1/2} \sqrt{1 + s_{i+1/2}^2} \, \rho_{i+1/2} \varepsilon_i$$

(32)

(note the distinction between the grid spacing ε_i and the permittivity of free space ε_o). The field F_i is constant along the ith ribbon. From the F_i's, the total current from the emitter can be found by summing over the current contributions from each ribbon that constitute the tip:

$$I(V_g) = 2\pi \sum_{i=1}^{N_{tip}} \sqrt{1 + s_{i+1/2}^2} \; \rho_{i+1/2} \, \varepsilon_i \, J(F_i) \; . \tag{33}$$

Finally, if the potential away from the electrode surfaces is needed, as for field lines and trajectories [13], then a useful approximation is to replace each ribbon by a ring of charge located at $\rho_{i+1/2}$, with a total charge Q_i. The potential at any point (ρ,z) can then be calculated by:

$$\phi(\rho,z) = \sum_{i=1}^{N} \frac{Q_i}{2\pi} \int_0^{2\pi} \frac{d\varphi}{\sqrt{\rho^2 + (z - z_{i+1/2})^2 + \rho_{i+1/2}^2 - 2\rho\,\rho_{i+1/2}\cos(\varphi)}} , \tag{34}$$

$$= \sum_{i=1}^{N} Q_i \, \frac{2}{\pi} \frac{K(p_i)}{\gamma_i}$$

where, as before, the ε_o-dependent factors are implicit in the Q's. Finally, the capacitances are found from the matrix equation [(t,b,g,a) refers to (*tip, base, gate, anode*), respectively]:

$$\begin{bmatrix} Q_t \\ Q_b \\ Q_g \\ Q_a \end{bmatrix} = \begin{bmatrix} C_{tt} & C_{tb} & C_{tg} & C_{ta} \\ C_{bt} & C_{bb} & C_{bb} & C_{bb} \\ C_{gt} & C_{gb} & C_{gg} & C_{ga} \\ C_{at} & C_{ab} & C_{ag} & C_{aa} \end{bmatrix} \cdot \begin{bmatrix} \phi_t \\ \phi_b \\ \phi_g \\ \phi_a \end{bmatrix} , \tag{35}$$

where $C_{ij} = C_{ji}$, although this is not shown explicitly. To evaluate the C's, all the potentials (ϕ_i) except one (ϕ_j) are variously set equal to 0; we then have $C_{ij} = Q_i/\phi_j$. The charges are found by summing over the ribbon charges (as in Eq. (32)), e.g., for the tip, $Q_{tip} = \sum_i Q_i$ for all $\{i \in tip\}$. An alternate approach, which is used here, is to calculate $C(V_g) = C_{tg} + C_t V_a/V_g$; C_{tg} will then be the y-intercept in a plot of C vs $1/V_g$, and the tip-to-gate capacitance is obtained without separately calculating the capacitance matrix.

THE SEMI-NUMERICAL MODEL

In the semi-numerical model, we desire to retain the simple elegance of Eq. (27) for the $I(V_g)$ relation. From the qualitatively correct behavior of λ_s (Eq. (17)) and F_{tip} (derivable from Eq. (24)), we are in a position to estimate the parameters that will most dramatically affect the $I(V)$ relations (the behavior becomes more quantitatively correct if the gate thickness parameter t is very small; when the Saturn model's charge ring location no longer matches the "mean" radius of the charge distribution on the gate, or when the anode influences Q_g, the approximation fails). In this section, we provide a numerical approach for obtaining a refined estimate of the λ and F_{tip} parameters by using results of a minimal set of boundary element computations, and thereby obtain the most expeditious means of calculating the A_{fn} and B_{fn} parameters and the tip-to-gate capacitance. In particular, we require an algorithm to calculate $F_{tip}(V_g)$ and $\lambda(V_g)$ from the boundary element model for use in Eq. (27), in place of the values calculated by the Saturn model. From the linearity of the field vs gate voltage relations, it is clear that for the field, we have

$$F_{tip}(V_g) = \beta_f V_g + Y_f \tag{36}$$

(in keeping with the field enhancement factor convention, ß is the slope). Although not so obvious analytically (although apparent graphically), we can also use

$$\lambda(V_g) = (\beta_\lambda / V_g) + Y_\lambda \, , \tag{37}$$

where the subscripts on ß and Y refer to the $\lambda(V_g)$ and $F(V_g)$ slopes and intercepts, respectively. A similar trick can be used to find $Q_s(V_g)$ to evaluate C_{tg} using the Saturn model, but this is deferred to a future work.

Because of the linearity of Eqs. (36) and (37) in V_g and its inverse, only two boundary element calculations are required to determine the ß and Y parameters for a given geometry, likewise with the calculation of C_{tg}. A table of these values for various geometries can then be constructed from which any particular geometry can be extrapolated. Ideally, the Fowler-Nordheim A and B parameters should be evaluated by performing a linear fit of $\ln[I/V_g^2]$ vs $1/V_g$ in the regime of interest. However, the semi-numerical model, in conjunction with the Saturn model, can be used to infer parametric dependencies of A and B on the geometry and work function. For example, assume that $v(y) \approx v_o - y^2$, and anode effects are negligible, i.e., $Y_f \approx 0$. From Eq. (27), we therefore identify

$$B_{fn} \approx \frac{4}{3}\sqrt{\frac{2m}{\hbar^2}} \frac{v_o}{\beta} \phi^{3/2} \, , \tag{38a}$$

which hearkens to the field enhancement factor typically used. An analytical approximation for A_{fn} is more problematic, due to the dependence of $F_n(\lambda, x)$ on the gate voltage (that A_{fn} must be V_g-dependent has been noted before [16,20]). For typical parameters, we have found that F_n satisfies $(x+n)^{-1}[1-\exp(-\lambda(x+n))] \le F_n(\lambda,x) \le \lambda/(1+\lambda)$, the boundaries representing the lower and upper ranges of the gate voltage. Thus, order of magnitude estimates of A_{fn} are bounded from below by:

$$A_{fn} \approx \frac{3}{64} \frac{N_c a_s^2 \beta^3}{t_o^2 v_o \pi \lambda} \sqrt{\frac{2}{m\phi^5}} \ V_g \exp\left(\frac{16}{3} Q \sqrt{\frac{2m}{\phi\hbar^2}}\right) \tag{38b}$$

for the small V_g case, and where the (f) subscript on β has been suppressed. For the large V_g case:

$$A_{fn} \approx \frac{1}{8} \frac{N_c a_s^2 \beta^2}{t_o^2 \pi(\lambda+1)\phi\hbar} \exp\left(\frac{16}{3} Q \sqrt{\frac{2m}{\phi\hbar^2}}\right) \tag{38c}$$

when the gate voltage approaches its upper limit. As indicated in Eq. (38b), a plot of A_{fn} vs V_g is approximately linear in the low gate voltage regime. Equation (38) is given for pedagogical purposes and for order-of-magnitude estimates. As a means of calculating the Fowler-Nordheim fit parameters in Eq. (11), the voltage dependence of A_{fn} in Eq. (38) alters the best estimates of the FN A and B parameters as would be obtained from a linear fit performed on Eq. (27) (Appendix A) in a given V_g regime; ignoring anode effects can cause differences.

Although the Saturn model can give poor *quantitative* estimates of the field enhancement factor β, the *qualitative* dependencies can be inferred. In the Saturn model, the field at the tip primarily varies to first order as the ratio of the charge on the gate ring with the product of the distance from

the tip to gate ring and the tip radius, i.e., $F_{tip} \approx Q_g / a_s\, r_g \equiv \beta V_g$, where we have assumed that the tip radius is much smaller than the ring radius. If we assume that the tip of the emitter sphere lies approximately within the ring plane, that the anode is negligible, and that the asymptotic form of Eq. (23b) is used, we find:

$$F_{\text{tip}} \approx \frac{\pi}{a_s \ln\left(8\,\dfrac{a_g}{t}\right)}\, V_g \,.$$

(38d)

At this point, t is an unknown parameter that can even vary with gate voltage, although it is related in some sense to the gate parameters. The coefficient of V_g is the "Beta factor" (β). The relationship between the field at the tip and the charge on the gate ring allows us to conclude from Eq. (38d) that

$$C_{tg} = \beta a_s^2 \approx \frac{\pi a_s}{\ln\left(8\,\dfrac{a_g}{t}\right)} \,.$$

(38e)

To reiterate, Eq. (38) shows the nature of the dependences of A_{fn}, B_{fn}, F_{tip}, and C_{tg} on material and geometry-dependent parameters. Generally, neglecting the anode and complications due to finite gate width, tip cone angle, and so on, causes the quantitative estimates based on the above equations to be not reliable except for particular cases. However, as qualitative descriptions, Eqs. (38a-e) are in fact useful; they suggest the manner in which capacitance, field, and so on vary with geometrical parameters.

NUMERICAL RESULTS

Objectives

In this section, we undertake six tasks:

- use statistical analysis with boundary element computations to examine experimental data to develop and determine the applicability of the methodology;
- identify where improvements can be made and under what circumstances the conditions requiring improvement arise;
- demonstrate that the analytic generalizations of the statistical and Saturn sections are predictive;
- define the protocol behind the application of the semi-numerical method;
- demonstrate the utility of the boundary element method for analyses beyond current-voltage characterization, i.e., trajectory determinations and field lines within the unit cell; and
- delineate the incorporation of the semi-numerical method into more extensive simulation programs.

Protocol for the Comparison of Theory with Experiment

To judge the utility of the boundary element model in correlating with experimental data, we compare the results of the boundary element simulation based on the geometry shown in Fig. 2 with experimental data from two sources: the first has been provided by the Massachusetts Institute of Technology Lincoln Laboratories [12] (Case 1), and the second is characteristic of the SRI "Low Frequency Cathode" discussed in the literature [9] (Case 2). The low gate voltage regime of the Case

1 experimental data was used in the least-squares fitting, (it has been argued that the high voltage regime is affected by space charge).

Several effects complicate the comparison of theory with experiment:

- the actual work function and effective tip radius can be, and are, affected by the history of operation of the FEA and the processing steps, e.g., "plasma cleaning," and contaminants present;
- the actual FEA surface is not smooth, as implied by the theoretical procedure—there is always the possibility of microprotrusions. The scale of the microprotrusions, or surface non-uniformities, will introduce another parameter into the theory.
- the experimental current per tip is obtained by taking the ratio of the total FEA current and the total number of tips in the array.
- the shape of the gate in the FEA is more complex than assumed in the model here (although this can be accounted for in the future by altering the geometrical parameterization);
- the position and potential of the "virtual anode" will not, in general, be at the same location and potential over a range of gate voltages, as we have assumed here (this can be accounted for in a more careful treatment); and
- the distribution of emitters in all probability is more complex than the simple distributions examined here.

The first two concerns are dealt with by appealing to "effective work functions" and "effective tip radii." Insofar as the work function of the tip is affected by contaminants, we treat it as an adjustable parameter (within bounds). Microprotrusions and nonspherical tips are dealt with analogously: the analysis here returns a length scale that is characteristic of the tips in question, not the actual tip radius. As there is some evidence that surface non-uniformities and conditions can enhance emission, we might expect that surface protrusions and conditions for FEAs made by different processes may nevertheless result in comparable effective tip radius estimates.

Regarding the position and potential of the anode: In simulations of FEA performance, the equipotential lines at a distance of a few gate hole diameters from the gate plane are seen to be approximately linear. We are therefore justified in replacing one of these equipotential lines with a "virtual anode" held at the same potential. This approach is of great utility in the present simulations due to the finite size of the unit cell and the desire to keep the computational requirements to a minimum, that is, we desire the simulations to run on a desktop computer. Furthermore, it is justified insofar as the effect of the anode is overshadowed by the gate (although it is not insignificant). However, the position and potential of the actual anode is usually not reported, or is uncertain, making the potential and location of the virtual anode a problem. In Case 1, the actual anode was reported to have been held at 100 V at a distance of 100 μm from the gate, from which we approximate that the virtual anode should be held at 0.5 V at a distance of 0.5 μm from the gate (the virtual anode is 3.33 gate diameters away from the gate plane). In Case 2, the potential of the anode was reported, but the anode was at an angle with respect to the gate plane; we therefore made a heuristic estimation as to the potential and distance away of the virtual anode.

To correlate theory with experiment, we perform the following adjustments to the geometry and material parameters in order to obtain correlation with experiment:

- The value of B_{fn} is estimated first by adjusting the tip radius until approximate agreement with experiment is achieved. This "agreement" should actually be below the experimentally observed value if we intend to augment the simulation with a statistical analyis.

- Depending on the statistical model used, we next endeavor to match the A_{fn} parameter by adjusting the distribution of tips. Typically, the wider the distribution, the more A_{fn} is decreased, but also, the more B_{fn} is increased (thereby explaining why we desire to undershoot the B_{fn} estimate above). The introduction of the statistical analysis parameters primarily reduces the A_{fn} value, and therefore is the primary means of accounting for the fact that the experimental current per tip is always smaller than the current characteristic of the unit cell (sometimes significantly).
- The statistical analysis generally changes the B_{fn} estimate. We therefore return to the first step, and, depending on circumstances, tweak the work function and the virtual anode estimates in addition to the tip radius, until correlation is obtained.

This procedure will not produce a unique A_{fn} and B_{fn} estimate, being ad hoc in its implementation. Nevertheless, we have found that for the experimental cases we have simulated, the allowable range of values for effective tip radius, work function, and virtual anode are rather constrained. For example, for the three distributions considered below, decreasing ϕ to decrease B_{fn} results in A_{fn} being made larger. The validity of the modeling effort is enhanced by this observation, as well as the observations that the work function converged upon is within the range of acceptable values, the effective tip radii are supported by TEM studies, and the distribution estimates are not too dissimilar from experimental expectations.

Finally, and importantly, note that by constraining the statistical distribution to be given by one parameter (% tips emitting, ΔB, or σ), odd results may occur. For example, if a half-Gaussian distribution for an array for which only a subset of otherwise highly uniform tips are working is assumed, a large σ value will be estimated in order to lower A_{fn} to the experimentally observed value. This will be compensated for by estimating a smaller unit cell B_o than actually characterizes the subset. In the absence of detailed knowledge of the distribution of tips, such problems are unavoidable. However, we note that for the experimental data considered, the width of the distribution of B's for the various distributions considered are similar, arguing against such anomalous situations.

Further improvement and vindication of the modeling effort will necessarily include information from beam diagnostics (especially with regard to the trajectory analysis), tip characterization, and array scaling behavior; all of these have experimental counterparts within the NRL program in vacuum microelectronics.

Experimental Results vs Boundary Element Model

Figure 3 shows the discretization of the conducting surfaces used in the boundary element (BE) approach for the Case 1 parameters (the Case 2 discretization would differ only in scale). Fine discretization occurs in those regions where the field variation is expected to be large (e.g., at the tip of the emitter, near gate edges, etc.). The parameters used in the BE simulation are given in Table 2, and correspond to the labeling in Fig. 2. The results of the simulation, and the comparison with experimental data, is given in Table 2 in the section "Statistical Boundary Element Simulation."

Three distributions were used in the comparison of theory with the cases identified in Table 2:

- *Delta function distribution:* tips that emitted were assumed to be identical. Consequently, only one value of B_{fn} is present in the distribution. The number of tips (or % tips emitting) was adjusted to achieve correlation between theory and experiment for the values of A_{fn} once B_{fn} was identified.
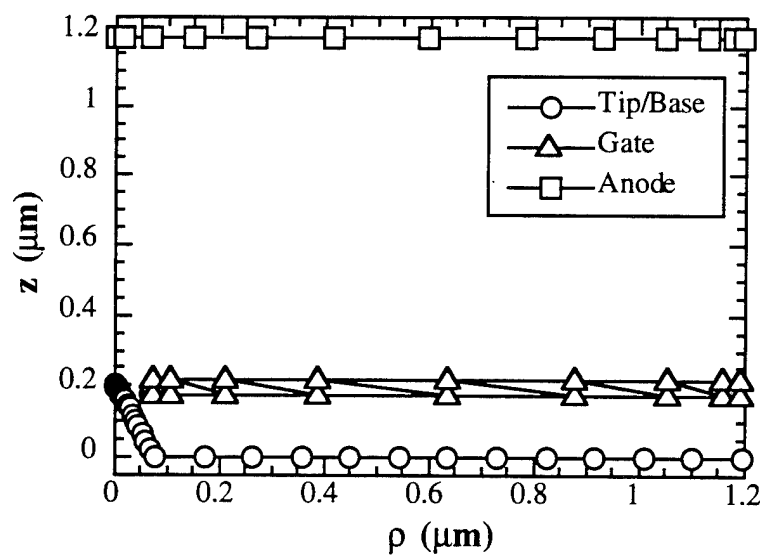
Fig. 3(a) — Boundary element discretization of conducting surface
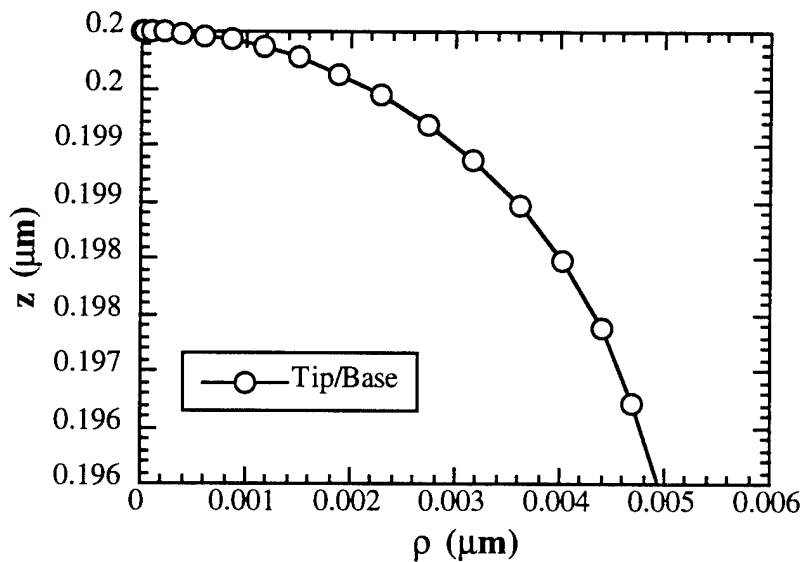of Case 1 (MIT) FEA unit cell

Fig. 3(b) — Close-up of FEA tip shown in Fig. 3(a). Note slight
curvature of gate edge

Table 2 — FEA Unit Cell Simulation Parameters

Symbol	Designation	Case 1 (MIT)	Case 2 (SRI)	Units
Parameterization				
Φ	work function	2.0	4.0	eV
t_h	tip height	0.2	1.3	μm
a_g	gate radius	0.075	0.6	μm
α	$\tan^{-1}$(base radius/tip height)	20	15	degrees
d_g	gate thickness	0.04	0.3	μm
d_{bg}	base to gate distance	0.195	1.15	μm
d_{ag}	gate to anode distance	0.5	3.0	μm
N	number of tips	975	1000	-
V_a	anode voltage	0.5	50	volts
	maximum gate voltage	23	78	volts
	minimum gate voltage	5	39	volts
Statistical boundary element simulation				
$A_{fn}\,(\delta)$	unit cell	318.7	2.06	μA/V^2
$B_{fn}(\delta)$	unit cell	93.2	423.8	volts
a_s	tip radius	30	40	Å
%	percentage tips emitting	65.85	22.82	%
$A_{fn}\,(\delta)$	delta distribution	356.9	5.6	μA/V^2
$B_{fn}(\delta)$	delta distribution	99.9	467.2	volts
a_s	tip radius	33	46	Å
ΔB	spread in B	27	300	volts
$A_{fn}\,(L)$	linear distribution	236.5	2.27	μA/V^2
$B_{fn}(L)$	linear distribution	100.5	466.5	volts
σ	distribution parameter	25	650	volts
$A_{fn}\,(hG)$	half-Gaussian distribution	231.3	1.17	μA/V^2
$B_{fn}(hG)$	half-Gaussian distribution	99.7	466.0	volts
Experimental parameterization (least-squares linear fit)*				
A_{fn}		235.0	1.28	μA/V^2
B_{fn}		100.7	467	volts

---

*   Data fit used a weighted least-squares line fit on the experimental points. For Case 1 (MIT): $9\ \text{V} \leq V_g \leq 15\ \text{V}$. For Case 2 (SRI): sample *53i+300-7Q* was fitted [9].

- *Linear distribution:* The B_{fn}'s were distributed as in Eq. (3). The value of ΔB was adjusted to fix A_{fn}.
- *Half-Gaussian:* The B_{fn}'s were distributed as in Eq. 4, where $B_- = B_o$. The value of σ was adjusted to fix A_{fn}.

The consequences of these three distributions with regard to effective tip radius are indicated in Table 2. The effective tip radius was assumed to be the same for both the unit cell and the linear and half-Gaussian distributions. These three widely disparate assumptions appear to result in comparable estimates of the tip radius, and in the similarity of the ΔB and σ estimates (the *full width at half maximum* of the half-Gaussian is $(1/2)\,\sigma\,\ln(2)$, which is comparable to ΔB). Note that a larger gate radius for Case 2 engenders a larger spread in the B_{fn} values, as intuitively expected. Note also that the similarity of effective tip radius for both Case 1 and Case 2 is suportive of the notion of surface nonuniformity. These estimates are comparible to the findings of Levine [8] and Cade et al. [34].

From the distribution in B_{fn}'s, we can infer the distribution in effective tip radius. From the tabulation of slopes and intercepts in the semi-numerical model as a function of tip radius, we can obtain a numerically empirical relation between the B_{fn}'s and the tip radii, analogous to Eq. (38). For brevity, consider the results for Case 1 only. Figure 4 shows the distribution of tips entailed by the assumed distribution in B's. The area under the linear and half-Gaussian curves is equal to 975 (the number of tips). Note: the Delta distribution has been scaled by 1/12, and there is a preponderance of tips with smaller radii. By using the fitted linear relations $B_{fn} \approx 31.23 + 2.078\,a_s$ and $A_{fn} \approx -90.66 + 13.54\,a_s$, in volts, and $\mu A/V^2$, respectively, we can calculate the total current contribution from each group of tips characterized by a given tip radius, as shown in Fig. 5. Notice that the total current, given by the area under each curve, is approximately the same. Again, compare the findings of Cade et al., for silicon emitters [34].

The work function used in Figs. 4 and 5 was for a cesiated tip, and was therefore taken to be 2.0 eV. If we assume that the geometry and distribution of tips remains identical, but we now consider the tips to be pure molybdenum with a work function of 4.35 eV, we can predict the performance of the resulting FEA (Fig. 6). On an FN plot, the $I(V)$ characteristics for the uncesiated case are, to a very good approximation, linear, and described by $A_{fn} = 22.90\ \mu A/V^2$ and $B_{fn} = 314$ V.

The low work function in Case 1 raises an interesting issue: Is approximating $J(F)$ in Eqs. (27) and (33) by $J_{FN}(F)$ valid? Figure 7 compares $J_{FN}(F)$ to the exact (Airy function solution) $J(F)$ [33]. For typical molybdenum parameters (and at room temperature), the Fowler-Nordheim estimate is typically too low by 20% or so (the discrepancy becomes worse at low fields, hence voltages, as a result of $J_{FN}(F)$ being a zero-temperature approximation). For the cesiated case, $J_{FN}(F)$ significantly overestimates the actual current at high fields. This is because the linearized WKB expression estimates that the transmission coefficient is greater than unity in the region where tunneling (and transmission over the barrier) is important. Using the correct $J(F)$ in the expressions for $I(V)$ will result in a bending over of the FN curve at high voltages (low V^{-1}). Consequently, as shown in Fig. 8, there is a small curvature downward at low (V^{-1}) when using the exact $J(F)$. Although the behavior of the experimental points in this regime is undoubtedly primarily due to space charge effects [34], some of it is due to the fact that nonlinearities are inherent in an FN plot of $J(F)$ in this regime. Finally, note that the exact curve is somewhat higher than that using $J_{FN}(F)$: as a result, the estimates of the spread in B parameters in Table 2 are smaller than would otherwise occur.
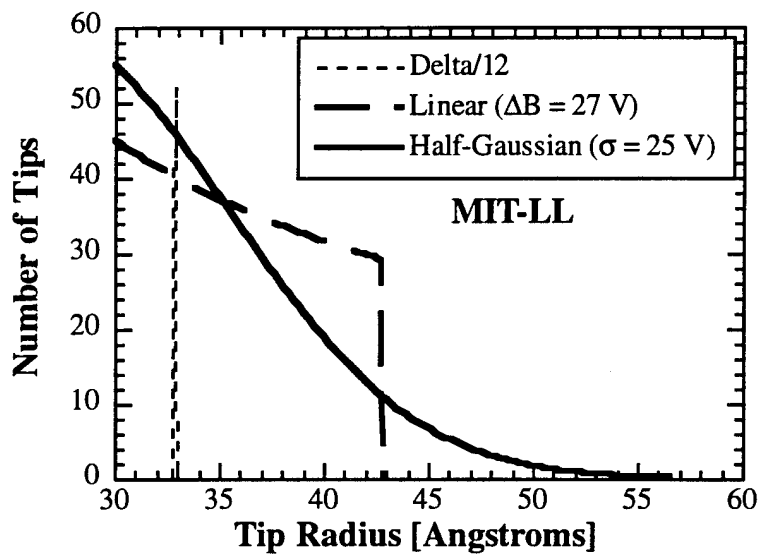
Fig. 4 — Distribution of emitters according to tip radius for Case 1 (MIT) parameters. Total number of emitters = 975. In the case of the Delta-function distribution, total number of *working* emitters = 630
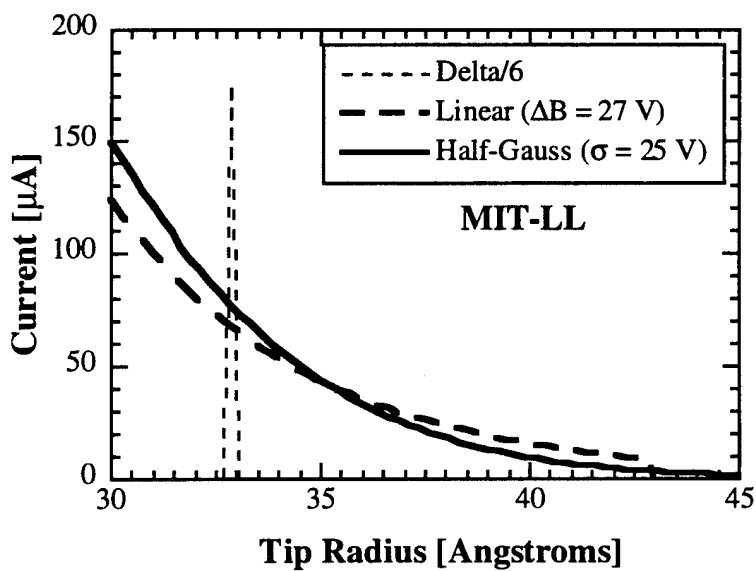

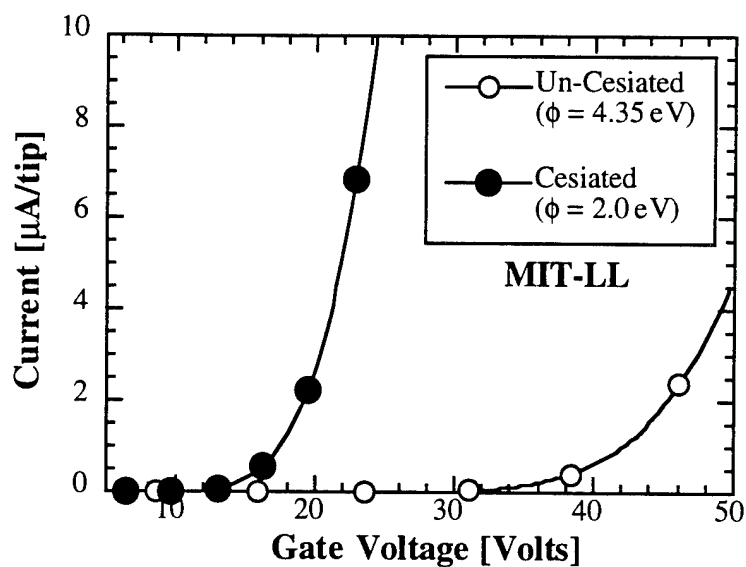Fig. 5 — Same as Fig. 4, but for total current per tip radius as a function of tip radius

Fig. 6 — Comparison of theoretical cesiated vs uncesiated FEAs for Case 1 (MIT)
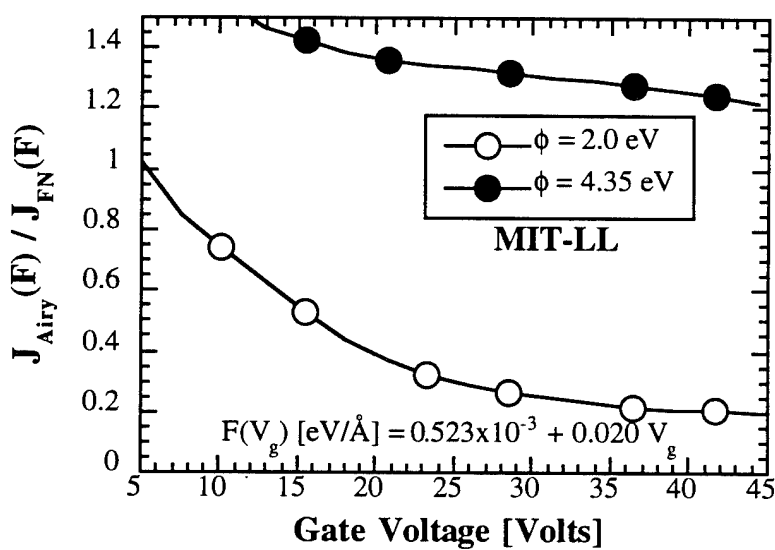parameters in the comparison of current with gate voltage

Fig. 7 — Comparison of Fowler-Nordheim approximation to $J(F)$ with exact solution
for Case 1 (MIT) parameters for cesiated and uncesiated work functions
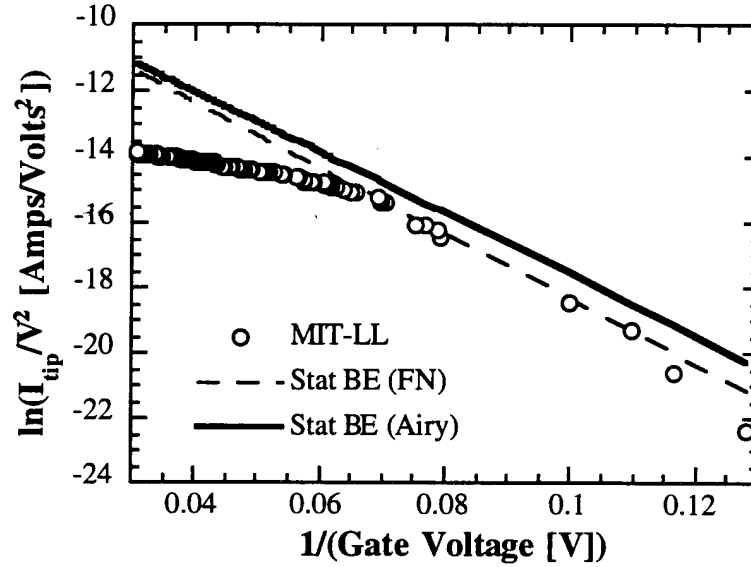
Fig. 8 — Fowler-Nordheim plot of experimental data and boundary element simulation. Solid line is for the calculation using the exact solution of $J(F)$, dotted line is for the calculation using the FN approximation to $J(F)$. Note the curvature at high gate voltages for the former

Validity of the Saturn and Semi-Numerical Model Approximations as Applied to the Unit Cell

The assumption that only the portion of the tip approximated by a sphere contributes to the total current, and that emission along the shank of the tip is negligible, is implicit in Eq. (27). In fact, the upper limit of the integral in Eq. (26) corresponds to an angle of 90°. It remains to be demonstrated that this approximation of the Saturn model, and hence, the semi-numerical model, is valid. Furthermore, the Saturn model itself cannot be used for field-on-axis estimates, as the emitter tip is close to the center of the gate plane (see Eq. (25) and discussions therein). Similarly, the Saturn estimates of λ are very small, whereas for the BE calculations, $\lambda \approx 0.32$ for a range of geometries. Nevertheless, the semi-numerical model works quite well. Figures 9 and 10 compare the full boundary element (BE) calculation for the parameters listed in Table 2 with the semi-numerical (SN) method, in which the linear fits shown in Eqs. (36) and (37) are used in the Saturn model equation for current, Eq. (27). As can be seen, the estimates are, in fact, quite close. We now explore the reasons for this. Note that all parameters not explicitly mentioned are assumed to be as given in Table 2 for the two cases considered.

The semi-numerical method implicitly assumes that the field variation along the surface of the emitter is governed by Eq. (17), albeit that the F_{tip} and λ parameter are given by the boundary element calculations, and are, in general, gate voltage-dependent. $F(\theta)$ is extracted from the boundary element data by defining $\tan(\theta) = (z_s/\rho_s)$, where θ is the polar angle of the equivalent sphere, and (ρ_s, z_s) are the coordinates along the surface of the actual emitter. Figures 11 and 12 show the $F(\theta)$ and $F(\rho_s)$ comparisons for MIT-LL and SRI geometries, respectively, as given in Table 2. It is seen that for "large" angles, the deviation between the BE method and the SN method grows.
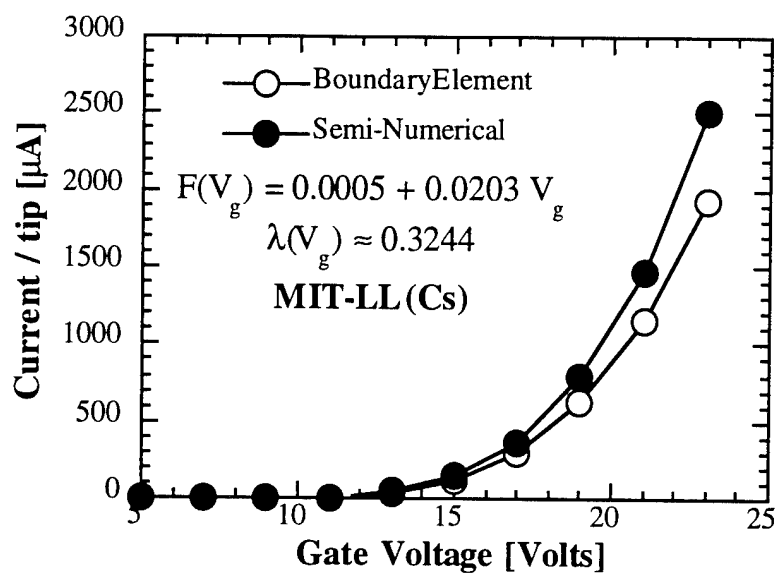
$$F(V_g) = 0.0005 + 0.0203\,V_g$$
$$\lambda(V_g) \approx 0.3244$$

MIT-LL (Cs)

Fig. 9 — Comparison of the boundary element and the semi-numerical methods (Case 1 parameters)

$$F(V_g) = 0.0748 + 0.00958\,V_g$$
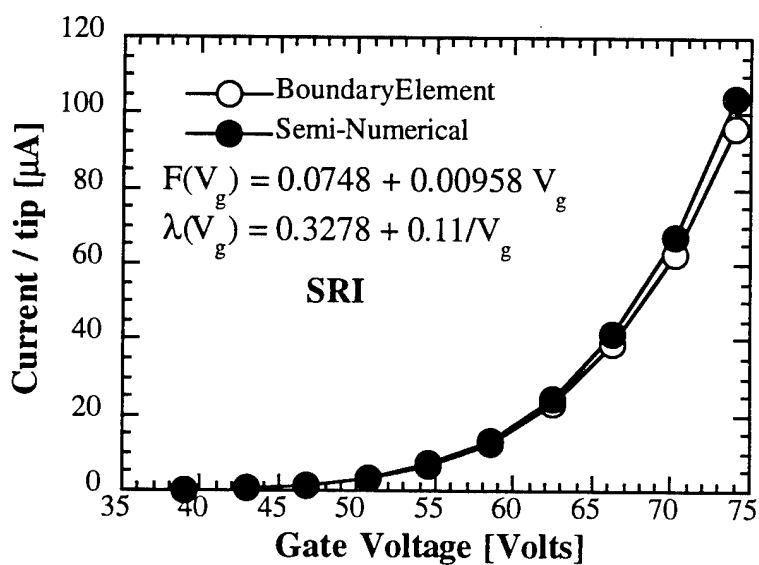$$\lambda(V_g) = 0.3278 + 0.11/V_g$$

SRI

Fig. 10 — Comparison of the boundary element and the semi-numerical methods (Case 2 parameters)
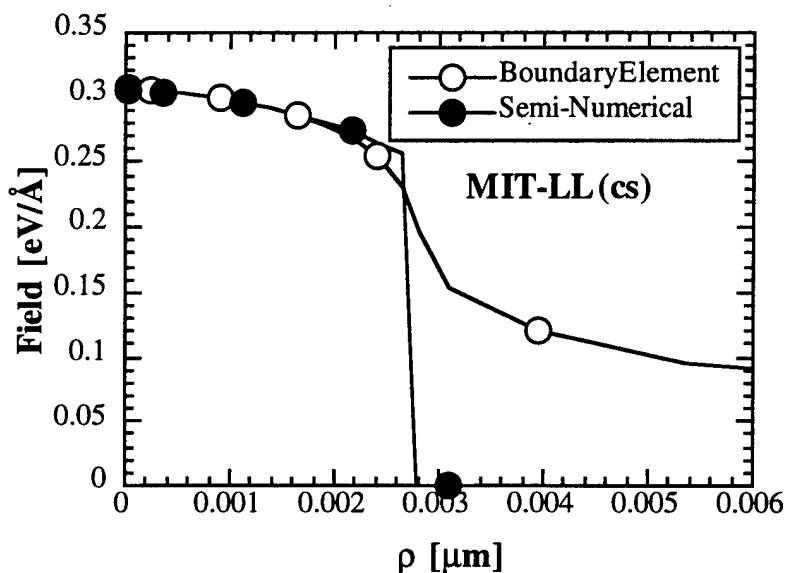
Fig. 11(a) — Field along the surface of the emitter as a function of cylindrical
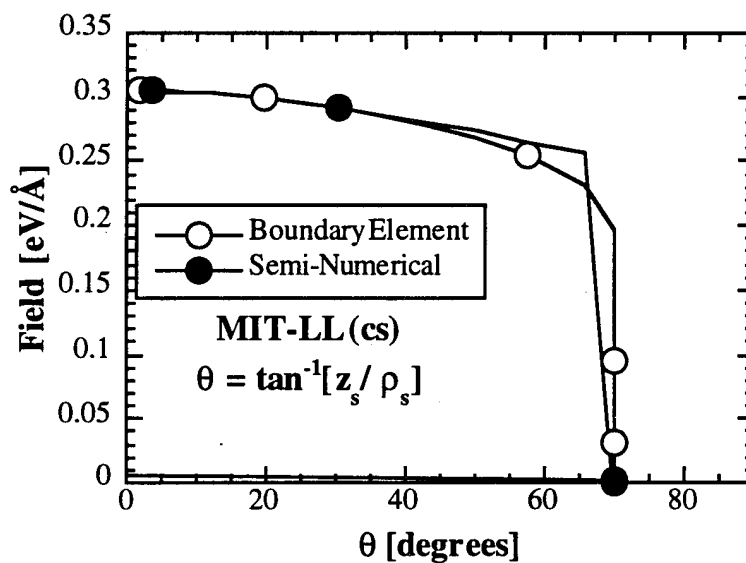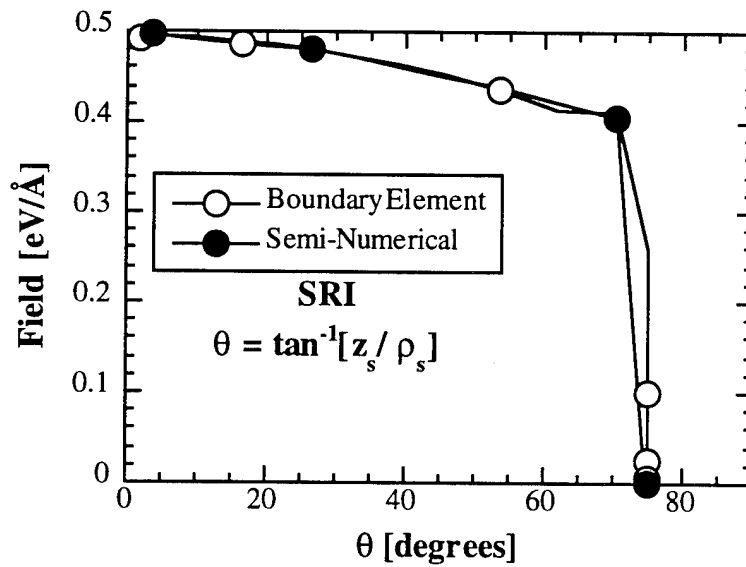coordinate ρ (Case 1 parameters (MIT))

Fig. 11(b) — Field along the surface of the emitter as a function of polar angle θ
(Case 1 parameters (MIT))
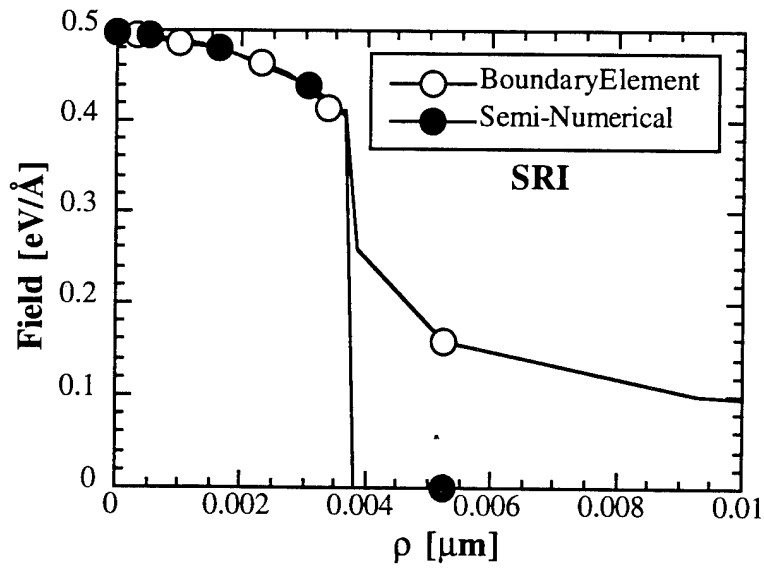
Fig. 12(a) — Field along the surface of the emitter as a function of cylindrical coordinate ρ
(Case 2 parameters (SRI))

Fig. 12(b) — Field along the surface of the emitter as a function of polar angle θ
(Case 2 parameters (SRI))

However, the current density falls rapidly with field, as shown in Figs. 13 and 14, and hence, the SN approximation is good despite the large angle behavior (in the latter, the field on axis tends to be mildly noisy; this noise can be diminished with proper discretization, and is in progress). The field along the shank of the emitter, while being non-zero, gives rise to a negligible current, and therefore need not be considered.

Figures 15 and 16 show the behavior of the B_{fn} and inverse field enhancement factor ($1/\beta$) as a function of tip and gate radius for the two cases in Table 2; as expected from Eq. (38), they are predominantly linear in tip radius. For small gate radii, the linearity in $\ln(a_g)$ is approximate and degrades as the gate radius grows, but for small gate radii (where the Saturn Model is presumed to be a better model), the linearity predicted by Eq. (38) is roughly correct. In Figs 15(b) and 16(b), both ($1/\beta$) and B_{fn} have the same qualitative dependence on gate radius. This indicates that B_{fn} is linear to a good approximation in ($1/\beta$), as can be shown explicitly, and as expected from Eq. (38).

Capacitance of FEA Unit Cell

Figure 17 shows the behavior of the ratio of C_{tg} with the parallel plate approximation given by

$$C_o = \varepsilon_o \frac{\pi a_g^2}{d_{bg} - \frac{1}{2} d_g} , \tag{39}$$

based on the dependencies indicated in Eq. (38). The x-axes in Fig. 17(a) differ from those in Fig. 17(b). In the former, the tip radius is varying, while in the latter, it is not. We see that the linearity prediced by Eq. (38) is in fact maintained in the boundary element calculations, although for varying gate radius, the linearity is apparent when the gate radius is small. Recall that the Saturn model, and hence, Eq. (38), relies on the assumption that the gate can be replaced by a ring of charge, and that this ring lies close to the edge of the gate. When the gate radius becomes large, the remainder of the gate, and the charges associated with it, cannot be as easily dismissed as we have done.

Note that what we are examining in Fig. 17 is the *tip-to-gate* capacitance C_{tg}, not the capacitance of the FEA unit cell overall. C_{tg} can be expected to be dominated by the parallel-plate-like capacitance between the gate and the base if the *tip-to-tip* separation is large. The charge residing on the base is large; in fact, the percentage of the charge residing on the tip alone of the total tip+base charge is 3.12% for Case 1 (MIT) and 5.7% for Case 2 (SRI). Consequently, the total capacitance between gate and (tip+base) dominates C_{tg}.

Field Distribution of FEA Unit Cell for Saturn and Boundary Element Models

In the Saturn model, the sphere representing the tip is charged. As a result, far from the sphere, the field due to that charge should fall off in a $1/r^2$ manner. The actual charge distribution is responsible for higher order (multipole) terms, but these can be neglected. In the boundary element model, two effects come into play: (a) the charge density is highest on the emitter tip, and (b) the field due to a charged ring along the axis of the ring goes as the inverse square of the distance from the observation point to any point on the ring. From these two observations, one can surmise that near the emitter tip, the field fall-off is roughly as predicted by the Saturn model.
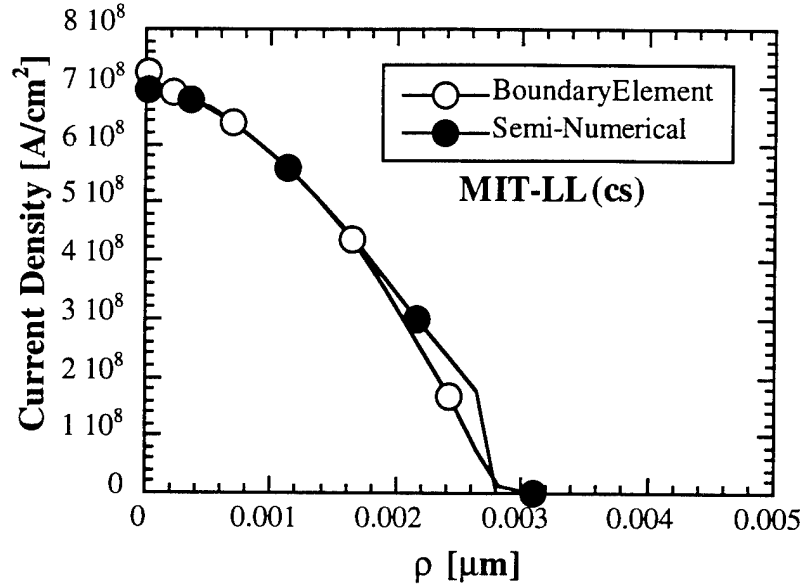
Fig. 13(a) — Current density along the surface of the emitter as function of cylindrical
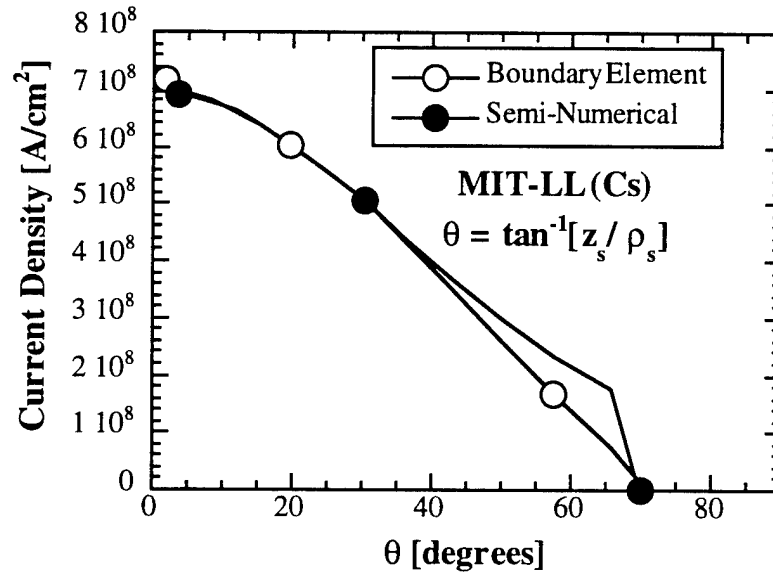coordinate ρ (Case 1 parameters (MIT))

Fig. 13(b) — Current density along the surface of the emitter as function of polar angle θ
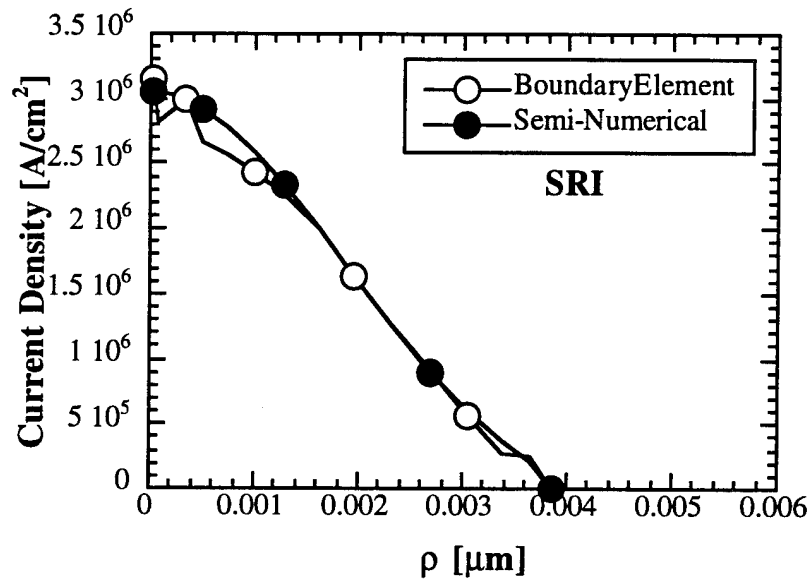(Case 1 parameters (MIT))

Fig. 14(a) —Current density along the surface of the emitter as function of cylindrical coordinate ρ (Case 2 parameters (SRI))

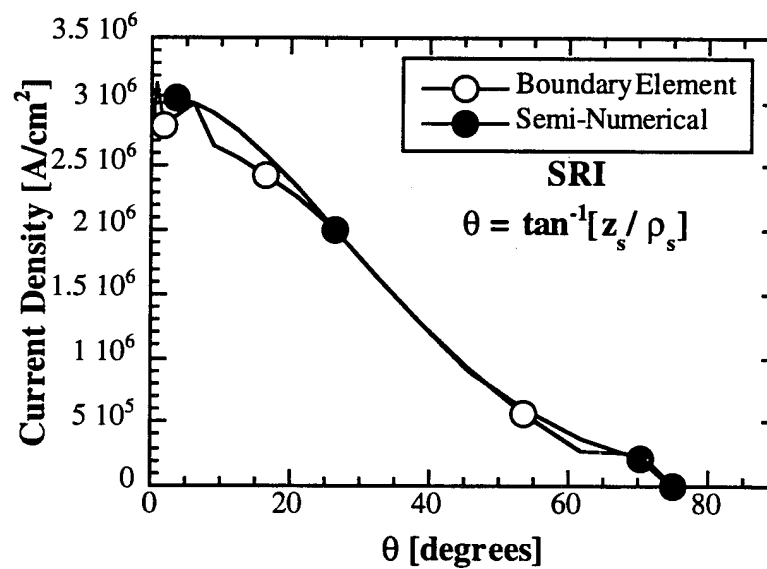Fig. 14(b) — Current density along the surface of the emitter as function of polar angle θ (Case 2 parameters (SRI))
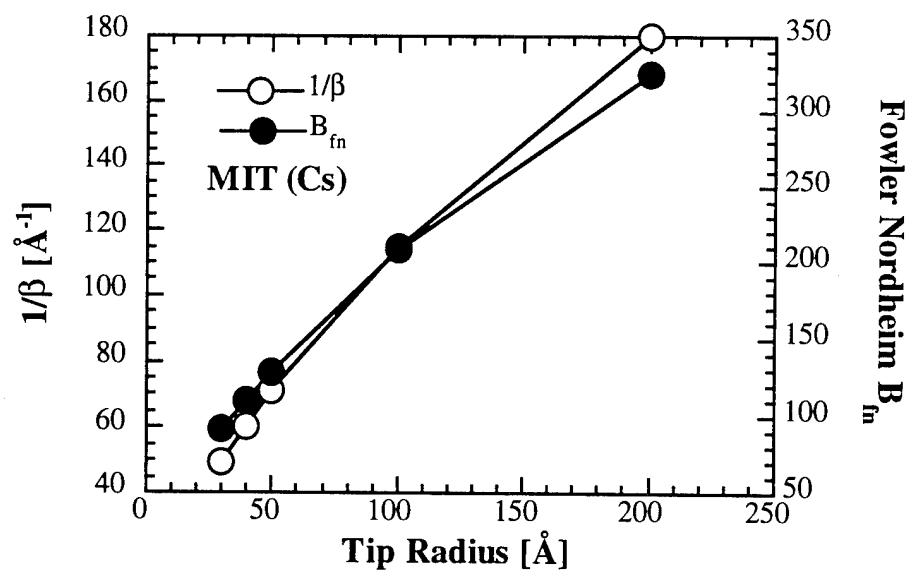
Fig. 15(a) — Field enhancement factor and Fowler-Nordheim B value as function of tip radius
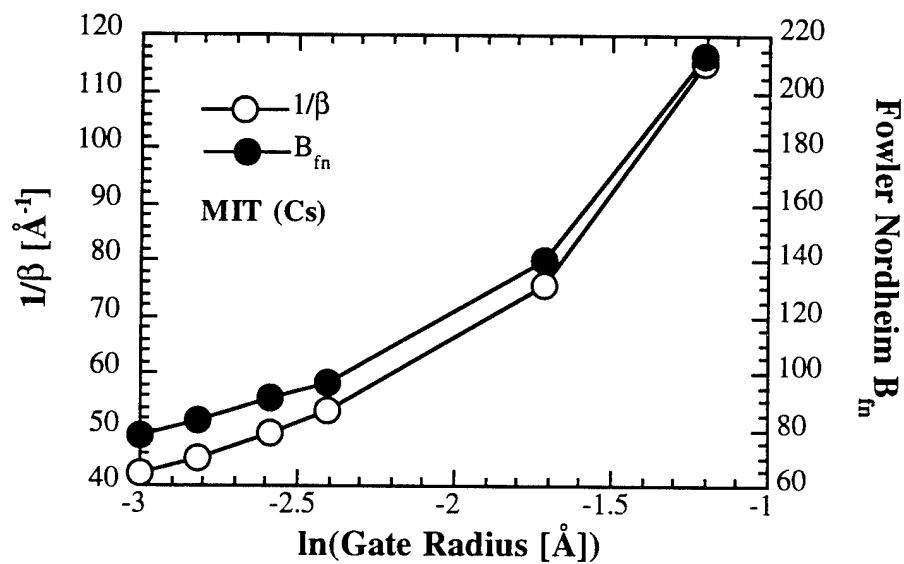(Case 1 parameters)

Fig. 15(b) — Field enhancement factor and Fowler-Nordheim B value as function of gate radius
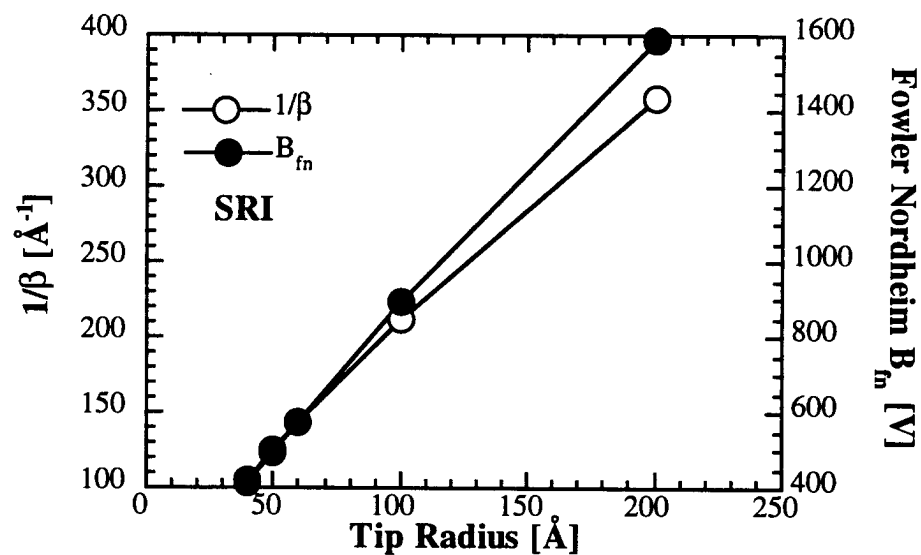(Case 1 parameters)

Fig. 16(a) — Field enhancement factor and Fowler-Nordheim B value as function of tip radius
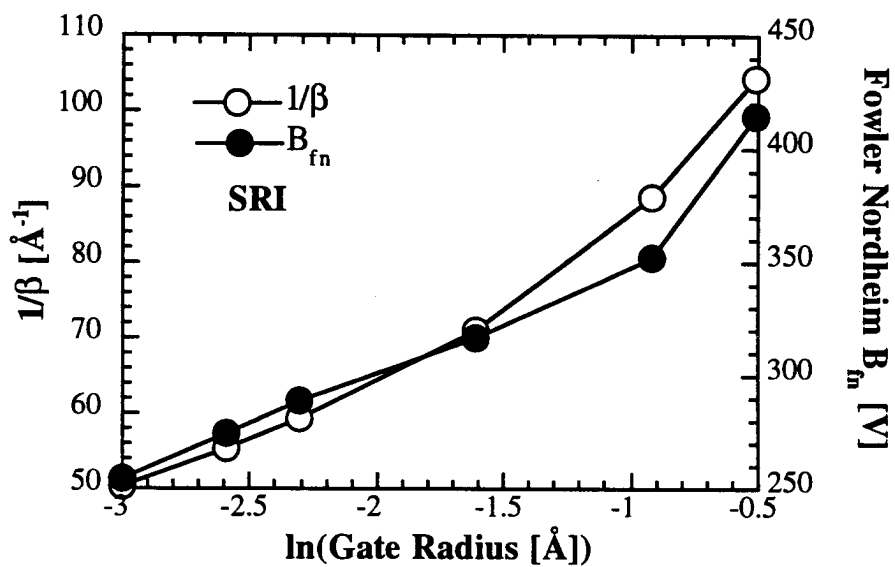(Case 2 parameters)

Fig. 16(b) — Field enhancement factor and Fowler-Nordheim B value as function of gate radius
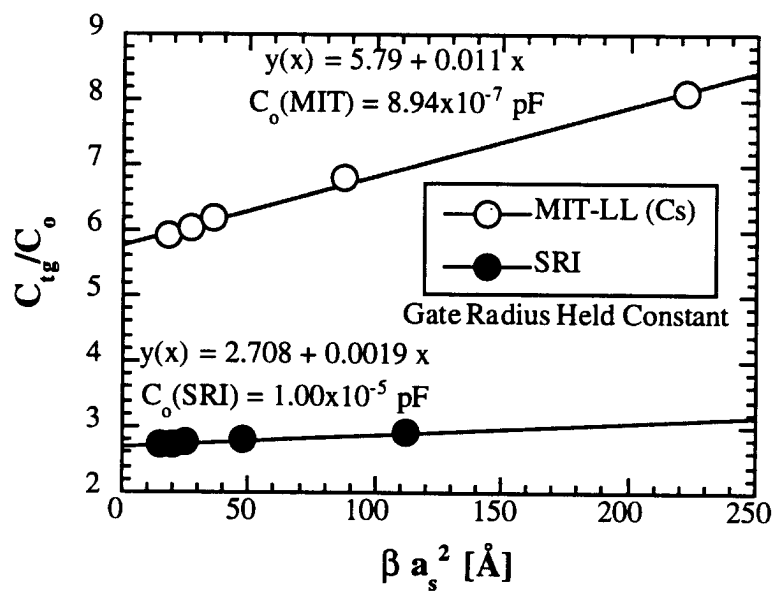(Case 2 parameters)

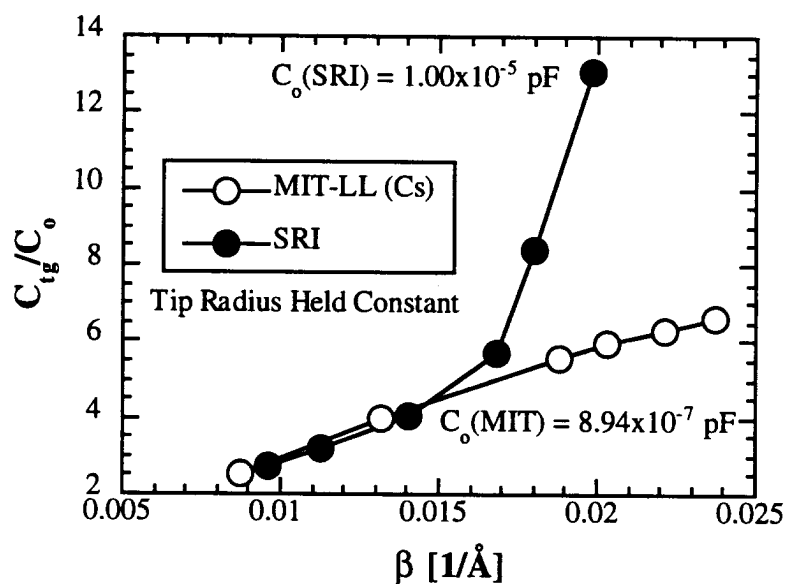Fig. 17(a) — Scaled capacitance for Cases 1 and 2 parameters (a) tip radius.

Fig. 17(b) — Scaled capacitance for Cases 1 and 2 parameters (b) field enhancement.

An expedient method for calculating both the potential and the field at any point in space not on a conducting surface is afforded by the ring representation of the charged surfaces, as in Eq. (34). On axis ($\rho = 0$), the expressions are particularly simple:

$$\phi(0,z) = \sum_{i=1}^{N} \frac{Q_i}{\left((z-z_i)^2 + \rho_i^2\right)^{1/2}} \tag{40}$$

$$F(0,z) = -\frac{\partial}{\partial z}\phi(0,z) = \sum_{i=1}^{N} Q_i \frac{z-z_i}{\left((z-z_i)^2 + \rho_i^2\right)^{3/2}} \; .$$

Figure 18 shows the field fall-off as calculated by Eq. (40) for the two cases considered in Table 2. Also shown is the Saturn approximation, which can be roughly recast as

$$F_{Saturn}(z) = F_o \left(\frac{a_s}{z}\right)^2 \; , \tag{41}$$

where F_o is the field at the tip, and a_s is the radius of the equivalent sphere. As seen in Fig. 18, Eq. (41) accounts for most of the behavior near the emitter tip.

Incorporation of Semi-Numerical Model into Larger Simulations

The length scale characteristics associated with the unit cell FEA analysis preclude the boundary element method, as presented here, from being used for an entire IOA simulation, although it is ideally suited for modeling conditions near the tip. Conversely, techniques using a finite-element analysis [21-23] are ideally suited for IOA simulation, whereas the discretization required for atomic-dimension tips is problematic. A method of combining the methods is indicated by observing that the boundary element method requires only a *virtual* anode to model conditions near the emitter tip. Consequently, a method for combining boundary element with finite-element is to use the latter to calculate or estimate the shape and potential of the virtual anode and then use the former to determine emission conditions. The field conditions in the immediate vicinity of the emitter are so extreme that space charge may not initially hinder the implementation of this algorithm, although past the virtual anode, where the field falls off considerably and the characteristic length scales are orders of magnitude larger, this will no longer in general be true. However, in the post-virtual-anode region, the finite-element method is ideally suited to deal with space charge effects. In practice, a few iterations between a finite-element simulation and the boundary element calculation may be required to correctly include the effects of space charge.

CONCLUSIONS

We have endeavored to present a simplified model of the FEA unit cell (the Saturn model), to show that the analytical formulae suggested by this model are valid, and to show how this model can be augmented (the semi-numerical model) in order to correlate with a full numerical solution based on the boundary element method of the field emitter unit cell. At present, attention has been restricted to refractory metal emitters characterized in the literature, but the method does not preclude an extension to semiconductor emitters. We have identified where the assumptions in both the analytic and numerical treatments may be in error, and have shown how to compensate for this.
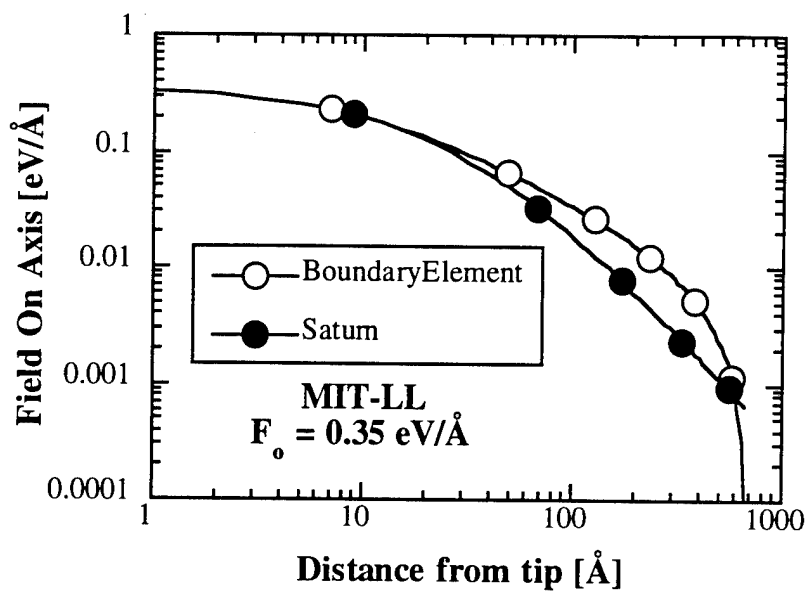
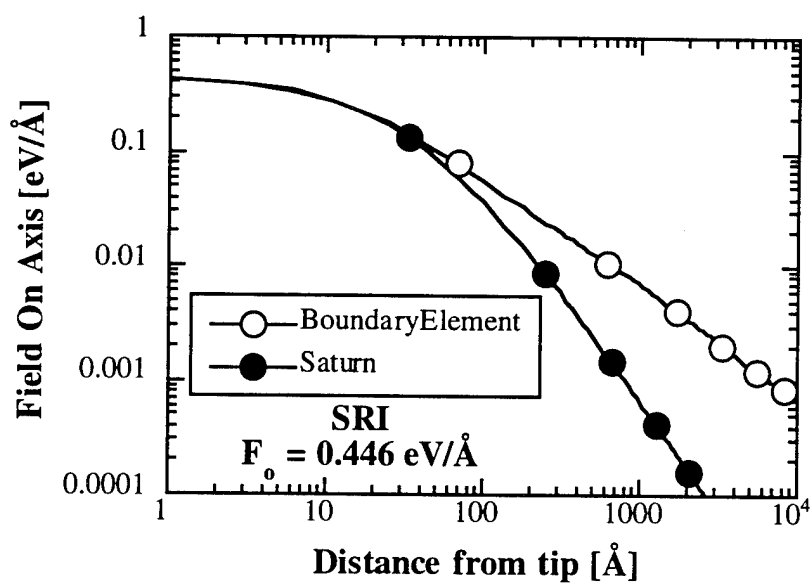Fig. 18(a) — Field on axis (Case 1 (MIT) parameters)

Fig. 18(b) — Field on axis (Case 2 (SRI) parameters)

Agreement between the qualitative behavior of the actual quantities of interest (i.e., current-gate voltage relations, capacitance, Fowler-Nordheim B_{fn} factors, beta factors, field and potential calculations within the unit cell, and so on) and the Saturn model vindicates the latter's simple representation of the FEA and its utility in understanding FEA unit cell behavior. The semi-numerical method demonstrates how the quantitative agreement can be restored between Saturn and boundary element through the introduction of slope and intercepts for F_{tip} and λ that are geometry dependent. This suggests the possibility of a library table-lookup algorithm to treat general FEAs without requiring a boundary element solution of the problem. Finally, we have shown how the statistical distribution of emitters can be examined to generalize from unit cell analysis to arrays in which tip non-uniformity may occur.

ACKNOWLEDGMENTS

REFERENCES

1. E. G. Zaidman and M. A. Kodis, "Emission Gated Device Issues," *IEEE Tran. Electron. Devices* **TED 38**, 2221 (1991).

2. J. P. Calame, H. F. Gray, and J. L. Shaw, "Analysis and Design of Microwave Amplifiers Employing Field-Emitter Arrays," *J. Appl. Phys.* **73**, 1485 (1993)

3. A. Ghis, R. Meyer, P. Rambaud, F. Levy, and T. Leroux, "Sealed Vacuum Devices – Fluorescent Microtip Displays," *IEEE Tran. Electron. Devices* **TED 38**, 2320 (1991).

4. M. A. Kodis, K. L. Jensen, E. G. Zaidman, B. Goplen, and D. N. Smithe, "Recent Developments in Inductive Output Amplifiers," NRL/FR/6840--95-9783, 1995.

5. A. Modinos, *Field, Thermionic, and Secondary Electron Spectroscopy* (Plenum, New York, 1984).

6. R. Gomer, *Field Emission and Field Ionization* (American Institute of Physics, New York, 1993).

7. W. D. Goodhue, P. M. Nitishin, C. T. Harris, C. O. Bozler, D. D. Rathman, G. D. Johnson, and M. A. Hollis, "Bright-Field Analysis of Field-Emission Cones Using High-Resolution Transmission Electron-Microscopy and the Effect of Structural-Properties," *J. Vac. Sci. Technol.* **B12**, 693 (1994).

8. J. D. Levine, "Statistical Analysis of Field Emitter Emissivity: Application to Flat Displays," Review "Le Vide, les Couches Minces," Supplement au N 271, March-April 1994.

9. C. A. Spindt, C. E. Holland, A. Rosengreen, and I. Brodie, "Field-Emitter-Array Development for High-Fequency Operation," *J. Vac. Sci. Technol.* **B11**, 468 (1993).

10. J. R. Taylor, *An Introduction to Error Analysis* (University Science Books, Mill Valley, CA, 1982), p.78.

11. J. Spanier and K. B. Oldham, *An Atlas of Functions* (Hemisphere Publishing Corp., New York, 1987) p. 385.

12. C. O. Bozler, R. A. Murphy, and M. Hollis, MIT-Lincoln Labs (private communication, May-June 1995).

13. P. M. Phillips, C. Hor, L. Malsawma, K. L. Jensen, and E. G. Zaidman, "Design of an Experiment to Determine the Electron-Beam Profile from Field Emitters," (submitted for publication).

14. P. H. Cutler, Jun He, N. M. Miskovsky, T. E. Sullivan, and B. Weiss, "Theory of Electron Emission in High Fields from Atomically Sharp Emitters: Validity of the Fowler-Nordheim Equation," *J. Vac. Sci. Technol.* **B11**, 387 (1993).

15. D. A. Kirkpatrick, A. Mankofsky, and K. T. Tsang, "Analysis of Field-Emission from 3-Dimensional Structures," *App. Phys. Lett.* **60**, 2065 (1992).

16. K. L. Jensen and E. G. Zaidman, "Field Emission from an Elliptical Boss: Exact Versus Approximate Treatments," *Appl. Phys. Lett.* **63**, 702 (1993).

17. L. G. Il'chenko and V. M. Ogenko, "Image Forces Near the Surface of a Semiconductor with a Space-Charge Region," *Surf. Sci. Lett.* **262**, L147 (1992)

18. V. G. Litovchenko, Y. V. Kryuchenko, L. G. Il'chenko, "Emission Properties of Field Cathode Tips and Structures with Quantum Wells," *J. Micromech. Microeng.* **3**, 74 (1993).

19. K. L. Jensen, "Improved Fowler-Nordheim Equation for Field Emission from Semiconductors," *J. Vac. Sci. Technol.* **B13**, 505 (1995).

20. D. Nicolaescu, "Physical Basis for Applying the Fowler-Nordheim J-E Relationship to Experimental I-V Data," *J. Vac. Sci. Technol.* **B11**, 392 (1993).

21. E. G. Zaidman, "Simulation of Field Emission Microtriodes," *IEEE Trans. Electron Devices* **TED 40**, 1009 (1993);

22. D. W. Jenkins, "Emission Area of a Field Emitter Array," *IEEE Trans. Electron Devices* **TED 40**, 666 (1993).

23. W. Dawson Kesling and Charles. E. Hunt, "Field Emission Device Modeling for Application to Flat Panel Displays," *J. Vac. Sci. Technol.* **B11**, 518 (1993).

24. D. Nicolaescu and V. Avramescu, "Field Emission Diode Characterization Through Model Parameters Extraction from Current-Voltage Experimental Data," *J. Vac. Sci. Technol.* **B12**, 749 (1994).

25. A. Renau, F. H. Read, and J. N. H. Brunt, "The Charge-Density Method of Solving Electrostatic Problems With and Without the Inclusion of Space-Charge," *J. Phys. E: Sci. Instrum.* **15**, 347 (1982).

26. R. L. Hartman, W. A. Mackie, and P. R. Davis, "Use of Boundary Element Methods in Field Emission Computations," *J. Vac. Sci. Technol.* **B12**, 754 (1994).

27. K. L. Jensen and E. G. Zaidman, "Analytic Expressions for Emission Characteristics as a Function of Experimental Parameters in Sharp Field Emitter Devices," *J. Vac. Sci. Technol.* **B12**, 778 (1994).

28. K. L. Jensen and E. G. Zaidman, "Analytic Expressions for Emission in Sharp Field Emitter Diodes," *J. Appl. Phys.* **77**, 3569 (1995).

29. T. Utsumi, "Keynote Address - Vacuum Microelectronics: What's New and Exciting," *IEEE Tran. Electron. Devices* **TED 38**, 2276 (1993).

30. L. Eyges, *The Classical Electromagnetic Field* (Dover, New York, 1972).

31. M. Hollis, MIT-Lincoln Labs (private communication, May-June 1995).

32. R. A. Murphy, M. Hollis, MIT-Lincoln Labs (private communication, May-June 1995).

33. K. L. Jensen and A. K. Ganguly, "Numerical Simulation of Field Emission and Tunneling: A Comparison of the Wigner Function and Transmission Coefficient Approaches." *J. Appl. Phys.* **73**, 4409 (1993).

34. C. O. Bozler, C. T. Harris, S. Rabe, D. D. RAthman, M. A. Hollis, and H. I. Smith, "Arrays of Gated Field-emitter Cones Having 0.32 μm Tip-to-tip Spacing," *J. Vac. Sci. Technol.* **12**, 629 (1994).

35. N. A. Cade, R. Johnston, A. J. Miller, and C. Patel, "Studies into the Emission Uniformity of Large Silicon Field Emitter Arrays," *J. Vac. Sci. Technol.* **B13**, 549 (1995).

Appendix A

Linearity of $I(V)$ on a Fowler-Nordheim Plot

Consider two limiting cases of the current-voltage relations characterized by Eq. (5). The "half-Gaussian" or "linear" distribution results in a general $<I(V)>$ relationship of the form:

$$I_n(V) = V^{2+n} \exp\left(A_o - B_o / V\right).$$ (A1a)

where n is some (not necessarily zero) integer. Note that while B_o corresponds to B_{fn}, A_o corresponds to $\ln(A_{fn})$. A Fowler-Nordheim plot of $I_n(V)$, in which $\ln(I_n/V^2)$ corresponds to the y-axis and $1/V$ to the x-axis, will be identically linear for $n = 0$, with a slope of $(-B_o)$ and a y-intercept of A_o, where A_o and B_o are constants. The "full-Gaussian" distribution results in a general $<I(V)>$ relationship of the form:

$$I_\sigma(V) = V^2 \exp\left(A_o - \frac{B_o}{V} + \left(\frac{\sigma}{2V}\right)^2\right).$$ (A1b)

For non-zero n and σ, the question arises as to how linear $\ln(I_n/V^2)$ or $\ln(I_\sigma/V^2)$ will appear.

Polynomial Least-Squares Fitting of General Functions

A function $y(x)$, continuous in a region $x_o - \delta \leq x \leq x_o + \delta$, is expanded in terms of Legendre polynomials. Let $y_m(x)$ be that polynomial of degree m, which minimizes the L_2 norm of $p_m(x) - y(x)$, where $p_m(x)$ is all polynomials of degree m or less [35]. We then have

$$y_m(x) = \sum_{k=0}^{m} C_k P_k(z)$$ (A2)

$$C_k = \left(k + \tfrac{1}{2}\right) \int_{-1}^{1} y(x) P_k(z)\, dz,$$

where $z = (x - x_o)/\delta$. There are several advantages to this approach. First, the Legendre polynomials satisfy $-1 \leq P_k(z) \leq 1$, so that from a numerical standpoint, Eq. (A2) is better behaved than a power series expansion. Second, $P_k(z)$ satisfies the recursion relation

$$(k+1)P_{k+1}(z) = (2k+1)\, z\, P_k(z) - k\, P_{k-1}(z)$$ (A3)

which, given $P_0(z) = 1$ and $P_1(z) = z$, allows the higher order Legendre polynomials to be easily evaluated for a given z.

The coefficient of linear correlation R gives a measure of how well $y(x)$ is approximated by $y_m(x)$. Let us define:

$$\sigma_{fg}^2 = \int_{x_o - \delta}^{x_o + \delta} \left(f - \langle f \rangle \right) \left(g - \langle g \rangle \right) dx$$

$$\langle f \rangle = \frac{1}{2\delta} \int_{x_o - \delta}^{x_o + \delta} f \, dx \quad .$$

(A4)

Then $R = \sigma_{xy} / \sqrt{(\sigma_{xx} \, \sigma_{yy})}$.

Table A1 – Fowler-Nordheim Linear Fit Parameters

Parameter	MIT-LL	SRI
Max V_{gate}	23 V	78 V
Min V_{gate}	5 V	39 V
x_o	0.1217	0.01923
δ	0.0783	0.00641
Unit Cell A_{fn}	318.7 $\mu A/V^2$	2.063 $\mu A/V^2$
Unit Cell B_{fn}	93.18 V	423.8 V

Least-Squares Fitting of Linear or half-Gaussian y(x)

For the particular choice $y(x) = - n \ln(x/x_o) + A - B x$, the C_k can be evaluated analytically. The first few have been found to be

$$C_0 = A - Bx_o + \frac{n}{2\delta}\left[-x_o S + \left(2 - U \right)\delta \right]$$

$$C_1 = -B\delta + \frac{3n}{4\delta^2}\left[\left(x_o^2 - \delta^2 \right)S - 2x_o\delta \right]$$

$$C_2 = \frac{5n}{12\delta^3}\left[-3x_o\left(x_o^2 - \delta^2 \right)S + 2\left(3x_o^2 - 2\delta^2 \right)\delta \right] \quad ,$$

(A5)

where

$$S = \ln\left(\frac{x_o + \delta}{x_o - \delta} \right); \quad U = \ln\left(1 - \left[\frac{\delta}{x_o} \right]^2 \right) \quad .$$

(A6)

The linearity of $y(x)$ is indicated by how close R^2 is to unity, or by the smallness of C_2 by comparison to C_0 and C_1. Finally, for a linear fit $(n = 1)$, in which $y_1(x) = A - B x$, the best A and B are found to be

$$\ln\left(A_{fn}\right) = C_0 - \frac{x_o}{\delta} C_1$$

$$B_{fn} = -\frac{C_1}{\delta} \ .$$

$$(A7)$$

Consider the two experimentally motivated cases discussed earlier, denoted MIT-LL [A1, A2] and SRI [A3]. Table A1 shows the relevant parameters, based on a least-squares fit of the experimental data and its relation to the unit cell modeling previously described. Tables 2 and A3 show the results of the best linear fit calculations. As indicated by both the value of C_2 and R, even for n large, $y_n(x)$ is still, to a good approximation, linear. A positive value of C_2 indicates that the curve is concave-up.

Table A2 – Fowler-Nordheim Linearity of $I_n(V)$

n	A_{fn} [$\mu A/V^2$]	B_{fn} [Volts]	C_0	C_1	C_2	R
Case 1: MIT-LL Unit Cell						
0	318.7	93.2	-19.40	-7.293	0.000	1.0000
1	1039	102.2	-19.32	-8.001	0.1698	0.9999
2	3386	111.3	-19.24	-8.709	0.3397	0.9995
3	1.104e+04	120.3	-19.16	-9.418	0.5095	0.9991
4	3.597e+04	129.4	-19.08	-10.13	0.6794	0.9986
5	1.172e+05	138.4	-19.00	-10.83	0.8492	0.9980
Case 2: SRI Unit Cell						
0	2.063	423.8	-21.24	-2.717	0.000	1.0000
1	5.850	477.0	-21.22	-3.058	0.03892	1.0000
2	16.59	530.3	-21.20	-3.399	0.07784	0.9998
3	47.06	583.5	-21.18	-3.740	0.1168	0.9997
4	133.5	636.7	-21.17	-4.081	0.1557	0.9996
5	378.6	689.9	-21.15	-4.422	0.1946	0.9994

Least-Squares Fitting of full-Gaussian y(x)

For the particular choice $y(x) = A_o - B_o x + D x^2$, where $D = \sigma^2/4$, the C_k can also be evaluated analytically; for $k > 2$, the C_k vanish. The remainder are given by

$$C_0 = A_o - B_o x_o + \frac{1}{3}D(\delta^2 + 3x_o^2)$$

$$C_1 = (-B_o + 2Dx_o)\delta$$

$$C_2 = \frac{2}{3}D\delta^2 \ .$$

$$(A8)$$

In contrast to Eq. (A6), non-zero σ will cause B_{fn} to decrease; the equation for $y(x)$ is a concave-up parabola. For the same parameters in Table A1, we can construct in Table A3 an analog to Table A2.

Table A3 – Fowler-Nordheim Linearity of $I_\sigma(V)$

σ [V]	A_{fn} [μA/V^2]	B_{fn} [Volts]	C_0	C_1	C_2	R
Case 1: MIT-LL Unit Cell						
.0	318.7	93.18	-19.39	-7.292	.0000	1.0000
5.0	294.2	91.66	-19.29	-7.173	.0255	1.0000
10.0	231.5	87.09	-18.97	-6.816	.1021	0.9999
15.0	155.3	79.48	-18.45	-6.221	.2297	0.9996
20.0	88.80	68.83	-17.71	-5.387	.4083	0.9983
25.0	43.27	55.14	-16.76	-4.315	.6380	0.9935
Case 2: SRI Unit Cell						
.0	2.063	423.8	-21.24	-2.717	.0000	1.0000
30.0	1.904	415.1	-21.16	-2.661	0.0061	1.0000
60.0	1.497	389.2	-20.90	-2.495	0.0247	1.0000
90.0	1.003	345.9	-20.46	-2.217	0.0555	0.9998
120.0	.5724	285.3	-19.86	-1.829	0.0986	0.9991
150.0	.2783	207.5	-19.08	-1.330	0.1541	0.9960

In this case, for a *given A_o and B_o*, the effects of a wider statistical distribution of B's, as represented by σ, results in a smaller best fit B_{fn} value. This is in constrast to the linear or half-Gaussian results. However, note that in the former case, B_o represents the *smallest B* value in the distribution, whereas in the latter, it represents the *mean* value.

REFERENCES

A1. C. O. Bozler, R. A. Murphy, and M. Hollis, MIT-Lincoln Labs (private communication, May-June 1995).

A2. C. O. Bozler, C. T. Harris, S. Rabe, D. D. RAthman, M. A. Hollis, and H. I. Smith, "Arrays of Gated Field-emitter Cones Having 0.32 μm Tip-to-tip Spacing," *J. Vac. Sci. Technol.* **12**, 629 (1994).

A3. David M. Young and Robert Todd Gregory, *A Survey Of Numerical Mathematics*, Vol. 1, (Dover, New York, 1973) pp. 318-324.

Appendix B

Chemical Potential and Temperature-Dependent Fowler-Nordheim Equation

The chemical potential and temperature-dependent Fowler-Nordheim equation for metallic parameters is given by

$$J_{\text{FN}}(F,\beta,\phi,\mu) = a_{fn} F^2 e^{-b_{fn}/F} \left(\frac{(c_{fn}\pi/\beta)}{\sin\left(c_{fn}\pi/\beta\right)} - [c_{fn}\mu + 1]e^{-c_{fn}\mu} \right)$$

$$a_{fn} = \frac{1}{16\pi^2\hbar\,\phi\,t(y)^2}$$

$$b_{fn} = \frac{4}{3\hbar}\sqrt{2m\phi^3}\,v(y) \tag{B1}$$

$$c_{fn} = \frac{2}{\hbar F}\sqrt{2m\phi}\,t(y) \quad ,$$

where $y^2 = 4QF/\phi^2$. Note that a_{fn} and b_{fn}, as defined here, are *not* independent of the field F. The functions $v(y)$ and $t(y)$ can be evaluated via integral definitions. Polynomials appropriate for numerical work are [B1]:

$$t(y) = \frac{1}{8\sqrt{2}}\pi\left[\left(3\,\{[(4298z+465)z+40]\,z+4\}\,z-8\right)z+4\right]$$

$$v(y) = \frac{3}{\sqrt{2}}\pi\,(\{-[3(665z+94)z+52]z-20\}z+4)z \tag{B2}$$

$$z(y) = \frac{(1-y)}{16} \quad .$$

It is common in the literature to take the zero temperature $(T \to 0)$ and infinite chemical potential $(\mu \to \infty)$ limit of Eq. (B1) (which amounts to neglecting the terms in parentheses), and approximate $t(y)$ by a constant and $v(y)$ as a linear function in y^2. By Taylor-expanding $v(y)$ about y_o and insisting that the coefficient of y^2 be unity, it can be shown that

$$t(y) \approx 1.05657$$
$$v(y) \approx 0.93685 - y^2 \tag{B3}$$

Equation (B3), however, is not the *least-squares* approximation, which can be shown to be:

$$t(y) = 1.06667 \tag{B4}$$
$$v(y) = 0.94199 - 0.96969y^2$$

In spite of the fact that Eq. (B4) is closer to the actual values of $v(y)$ and $t(y)$, the form of Eq. (B3) is often used because of the simplicity of the y^2 coefficient.

Appendix C

Field Enhancement Effects Due To Surface Curvature

Boss on Plane

Consider an infinite planar conductor with a hemispherical boss of radius a on the surface. Far from the conductor, let the field F in the z direction be constant. Using a Legendre polynomial expansion method [C1], the potential everywhere is

$$V(r,\theta) = V_o - F\, r \cos\left(\theta\right)\left[1 - \left(\tfrac{a}{r}\right)^3\right], \tag{C1}$$

where $z = r\cos(\theta)$. The field along the surface of the boss ($r = a$) is then

$$\vec{F}(a,\theta) = -\left.\nabla V(r,\theta)\right|_{r=a} = 3\, F \cos\left(\theta\right). \tag{C2}$$

The field at the tip of a protrusion is therefore enhanced by a factor of 3 compared to the field far away from the boss.

Two-Dimensional Hyperbolic Wedge (Diode)

For generalized coordinates (q_1, q_2, q_3), the gradient and the Laplacian are given by [C2]

$$
\begin{aligned}
h_i^2 &= \partial_i^2 x + \partial_i^2 y + \partial_i^2 z \\
\nabla &= \sum_{i=1}^{3} \hat{i}\, h_i^{-1}\, \partial_i \\
\nabla^2 &= \left(h_1 h_2 h_3\right)^{-1} \sum_{i,j,k=1}^{3} \tfrac{1}{2}\left(1 + \varepsilon_{ijk}\right)\varepsilon_{ijk}\, \partial_i\left(\frac{h_j h_k}{h_i}\, \partial_i\right),
\end{aligned}
\tag{C3}
$$

where ε_{ijk} is the Levi-Civita symbol, and $(q_1, q_2, q_3) = (x, y, z)$ in Cartesian coordinates. In 2-dimensional hyperbolic coordinates (α, β, γ) we have:

$$
\begin{aligned}
x &= a_h \sinh\left(\alpha\right)\sin\left(\beta\right) \\
y &= a_h \cosh\left(\alpha\right)\cos\left(\beta\right) \\
z &= \gamma,
\end{aligned}
\tag{C4}
$$

where a_h is the distance from the origin to the focus of the hyperbola defined by constant β. Solving $\nabla^2\psi = 0$ under the boundary conditions $\psi(\beta=\beta_o) = 0$ ("wedge") and $\psi(\beta=\pi/2) = V_o$ ("anode") is a straightforward problem and results in

$$\psi(\beta) = V_o \frac{(\beta - \beta_o)}{\left(\frac{\pi}{2} - \beta_o\right)}$$

$$\vec{F}(\alpha,\beta) = (-\hat{\beta}) \frac{V_o}{a_h\left(\frac{\pi}{2} - \beta_o\right) \sqrt{\sinh^2(\alpha) + \sin^2(\beta)}}. \tag{C5}$$

Define the radius of curvature of the wedge as $\partial_x^2 y\,|_{x=0} = 1/a_s$, and the distance from the wedge to the anode as z_o, such that $\tan^2 \beta_o = a_s / z_o$. In the limit that β_o is small, the field at the tip goes as $F_{tip} \approx 2V_o / \pi\sqrt{(a_s z_o)}$.

Three-Dimensional Hyperbolic Tip (Diode)

Consider a hyperbolic tip with rotational symmetry, for which

$$x = a_h \sinh(\alpha) \sin(\beta) \cos(\gamma)$$
$$y = a_h \sinh(\alpha) \sin(\beta) \sin(\gamma) \tag{C6}$$
$$z = a_h \cosh(\alpha) \cos(\beta).$$

Invoking Eq. (C3), letting $\psi = X(\alpha)\,Y(\beta)\,Z(\gamma)$, and exploiting the independence of ψ on γ gives

$$\left[\partial_\alpha\left(\sinh(\alpha)\,\partial_\alpha\right) - n(n+1)\sinh(\alpha)\right] X(\alpha) = 0$$

$$\left[\partial_\beta\left(\sin(\beta)\,\partial_\beta\right) + n(n+1)\sin(\beta)\right] Y(\beta) = 0 \tag{C7}$$

for which

$$X_n(\alpha) = a\, P_n(\cos(i\alpha)) + a'\, Q_n(\cos(i\alpha))$$
$$Y_n(\beta) = b\, P_n(\cos(\beta)) + b'\, Q_n(\cos(\beta)), \tag{C8}$$

where $P_n(x)$ and $Q_n(x)$ are Legendre polynomials of the first and second kind, the a's and b's are constants. Invoking the boundary conditions, analogous to the wedge, that the tip is at zero potential and the anode at V_o, we find that $n = 0$ and

$$Q_o(x) = \tfrac{1}{2} \ln\left(\frac{1+x}{1-x}\right)$$

$$\psi(\beta) = V_o\left[1 - \frac{Q_o\big(\cos(\beta)\big)}{Q_o\big(\cos(\beta_o)\big)}\right] \tag{C9}$$

$$\vec{F}(\alpha,\beta) = (-\hat{\beta}) \frac{V_o}{Q_o\big(\cos(\beta_o)\big)} \frac{1}{a_h \sin(\beta) \sqrt{\sinh^2(\alpha) + \sin^2(\beta)}}.$$

In the limit of small β_o, the field at the tip goes as

$$F_{tip} \approx \frac{2\,V_o}{a_s \ln\left(4\frac{z_o}{a_s}\right)}. \tag{C10}$$

Note that this is a slightly weaker dependence on the tip radius than in Eq. (38d) for the triode, as the ln-term in Eq. (C10) contains a factor of a_s. Invoking the polar coordinate-based parametric

representation introduced in Eq. (17), we find that $\lambda \approx 1/\cos^2(\beta_o) \approx 1$. Equation (27) may now be used to estimate the current from a hyperbolic diode.

REFERENCE

C1. G. Arfken, *Mathematical Methods for Physicists,* 3rd edition (Academic Press, Orlando, Florida, 1985).